Title

Effective area calibration of the RGS

Prepared by : Jelle Kaastra, Cor de Vries & Jan-Willem den Herder SRON June 19, 2018

Stored :

Distribution

SRON, ESAC

Document change record

Issue	Date	Changed Section	Description of Change
1	August 1, 2014	All	First issue
2	June 19, 2018	All	Summary report

References

Applicable documents

AD#	Doc. Reference	Issue	Title

Reference documents

RD#	Doc. Reference	Issue	Title

Contents

1 Introduction . . . 4

2 Sources and datasets used . . . 4
- 2.1 Preliminary remarks . . . 4
- 2.2 Data sets used . . . 4
- 2.3 Data processing . . . 7

3 Scattering: the response at short wavelength . . . 7

4 A higher resolution look to the RGS calibration: better models . . . 9
- 4.1 Introduction . . . 9
- 4.2 Improvements in the spectral models: Galactic absorption . . . 9
- 4.3 Improvements in the spectral models: spectral curvature . . . 10
- 4.4 Results of the new fits . . . 11

5 Deriving the effective area corrections for RGS1 and RGS2 . . . 12
- 5.1 Method . . . 12
- 5.2 Results . . . 13
- 5.3 Quality of the correction factors . . . 13
- 5.4 Some sanity checks . . . 14

6 Some possible physical effects . . . 15
- 6.1 Near the oxygen edge . . . 15
- 6.2 Hydrazine contamination? . . . 15
  - 6.2.1 Transmission near the nitrogen edge . . . 15
  - 6.2.2 Reflection . . . 16

7 Conclusions . . . 20

8 Some examples of the correction factors . . . 20

9 Appendix: Plots of fits to the correction parameters . . . 24

1 Introduction

From a preliminary analysis a few years ago, there were indications that the ratio of the fluxes derived by RGS1 and RGS2 changes with time, suggesting the presence of a calibration issue. Since then, the RGS data analysis tools have been improved significantly, and now for instance full data analysis in wavelength space without remaining artefacts is possible. This has great advantages, as it allows to compare different RGS spectra directly without the need to rebin (different RGS1 or 2, or different spectral orders).

Therefore it is now possible to re-investigate the problem further.

Furthermore, the work by Kaastra et al. (2011, A&A 534, A37) showed that there are significant remaining "wiggles" in the effective area. This could be shown by comparing the RGS1 with RGS2 spectra of Mrk 509. However, the underlying spectrum of Mrk 509 is rather complex, and much better statistics can be achieved by using the blazar spectra of sources like Mrk 421 and PKS 2155-304.

Finally, up to now the calibration of the second order spectra has not been one of the prime focuses of the RGS calibration. However, in the band below 18 Å, both second orders added together offer an effective area comparable to a single first order spectrum. Using second order spectra therefore helps enhancing the significance of spectral features, while at the same time they offer twice the spectral resolution compared to first-order spectra.

2 Sources and datasets used

2.1 Preliminary remarks

We use for this work data from Blazars. In an earlier version of this work, we have used a subsample of these data and made a comparison with EPIC-pn data. This investigation is not reported here in detail, but the main conclusions were as follows.

1. There is about 2–3% scatter between the RGS/pn flux ratio for different observations of different targets at 1 keV, which is much larger than the statistical uncertainty on this ratio.
2. This scatter occurs for all EPIC filters and all sources.
3. There is no significant time-dependence of the RGS/pn flux ratio at 1 keV.

Factors that may affect this are the different sensitivity ratio of RGS and EPIC at different energies, EPIC pile-up corrections (the cores of the psfs show strong pile-up in EPIC), and other factors. Since we did these comparisons, the EPIC calibration has evolved further, and to properly assess the comparison of RGS with EPIC this analysis should be redone, which is outside the scope of the present document.

2.2 Data sets used

We have used the available data of the blazars Mrk 421, PKS 2155-304, 3C 273 and H 1426+428. We took care to include only those datasets that were on-axis in the cross-dispersion direction, and for which both RGS1 and RGS2 data exist. See Table 1 for more info.

Table 1: Observation log. Source IDs: 1 = Mrk 421, 2 = PKS 2155-304, 3 = 3C 273, 4 = H 1426+428. The second column gives the XMM-Newton orbit, the third column the obsid, then the normalisation and photon index for a simple absorbed power-law fit of the RGS data over the RGS band; the norm is here 4π times the number of photons $\mathrm{m^{-2}s^{-1}keV^{-1}}$ at 1 keV; next the exposure time in ks for RGS1, then a number related to the number of counts in the spectrum, namely the $^{10}\log$ of the product of normalisation and exposure time (with exposure time now in s); finally, an indication for the offset in the dispersion direction, namely $\Delta \equiv (\lambda_{\max} - 38.195)/0.01$ with $\lambda_{\max}$ the maximum wavelength in Å that is present in the spectrum.

Id	orb	obsid	norm	Γ	t (ks)	$^{10}\log(\mathrm{norm}\times t)$	Δ
1	84	0099280101	23476	2.18	36	8.92	-2
1	84	0099280101	19156	2.29	27	8.71	-2
1	165	0099280201	8569	2.45	37	8.50	0
1	171	0099280301	28005	2.19	49	9.14	1
1	171	0099280501	32336	2.08	21	8.83	1
1	259	0136540101	20743	2.26	37	8.89	-1
1	440	0153950601	9578	2.56	39	8.57	30
1	546	0136541001	14574	2.33	71	9.01	0
1	637	0158970101	15113	2.49	43	8.81	0
1	640	0158970701	8533	2.61	49	8.62	2
1	720	0150498701	38486	2.21	49	9.27	-2
1	733	0162960101	18525	2.25	30	8.75	0
1	807	0158971201	41925	1.99	66	9.44	-1
1	1084	0158971301	37483	2.30	60	9.35	-1
1	1170	0302180101	26405	2.15	42	9.04	-1
1	1184	0411080301	49749	2.02	46	9.36	0
1	1280	0411080701	14436	2.52	19	8.43	0
1	1280	0411080801	13603	2.53	11	8.17	5
1	1357	0510610101	12373	2.60	25	8.49	-1
1	1358	0411081301	11615	2.62	19	8.34	-2
1	1358	0411081401	12616	2.60	9	8.05	5
1	1358	0411081501	13299	2.57	9	8.07	3
1	1358	0411081601	12845	2.56	9	8.05	-4
1	1358	0411081701	12790	2.56	7	7.95	-6
1	1455	0411081901	19673	2.42	19	8.57	-1
1	1455	0411082001	22476	2.38	9	8.33	6
1	1455	0411082101	21774	2.41	12	8.41	3
1	1455	0411082201	20930	2.41	9	8.27	-4
1	1455	0411082301	20999	2.42	14	8.46	-6
1	1552	0411082701	64141	2.30	11	8.84	-2
1	1640	0560980101	19861	2.49	71	9.15	6
1	1732	0560983301	19232	2.60	55	9.03	5
1	1820	0411083201	34981	2.24	53	9.27	7
1	1904	0656380101	30172	2.25	41	9.09	6
1	2001	0656380801	20979	2.31	40	8.93	6
1	2002	0656381301	16133	2.53	36	8.76	6
1	2094	0658800101	11706	2.59	30	8.54	-1
1	2095	0658800301	11458	2.39	28	8.50	2

Continued on next page

Continued from previous page

Id	orb	obsid	norm	Γ	t (ks)	$^{10}\log(\text{norm}\times t)$	Δ
1	2096	0658800501	9235	2.56	18	8.21	5
1	2192	0658800801	5320	2.75	26	8.15	7
1	2195	0658801201	6790	2.54	16	8.05	-7
1	2635	0670920301	30560	2.48	15	8.66	-2
1	2636	0670920401	19506	2.61	17	8.52	-2
1	2637	0670920501	25973	2.39	17	8.64	-2
2	174	0080940101	4069	2.69	59	8.38	-2
2	174	0080940301	3288	2.76	60	8.29	-1
2	362	0124930301	8558	2.65	90	8.89	2
2	450	0124930501	3782	2.55	102	8.59	-1
2	545	0124930601	2867	2.59	114	8.52	0
2	724	0158960101	2120	2.85	27	7.76	-1
2	908	0158960901	2397	2.87	29	7.84	-1
2	908	0158961001	3217	2.77	40	8.11	-1
2	993	0158961101	4442	2.64	29	8.11	-1
2	1095	0158961301	4714	2.71	60	8.45	0
2	1171	0158961401	1836	2.69	65	8.07	-1
2	1266	0411780101	2682	2.64	100	8.43	-1
2	1349	0411780201	4613	2.77	68	8.49	-2
2	1543	0411780301	5463	2.68	61	8.52	-2
2	1734	0411780401	3578	2.87	65	8.36	-2
2	1902	0411780501	1843	2.79	71	8.11	-2
2	2084	0411780601	3053	2.56	64	8.29	-2
2	2268	0411780701	708	2.85	57	7.60	-2
2	2449	0411782101	1579	2.74	76	8.08	-2
2	2542	0727770101	1724	2.60	95	8.22	4
2	2631	0727770501	1900	2.76	88	8.22	6
2	2633	0727770901	1676	2.82	64	8.03	-2
2	2632	0727771001	1498	2.74	39	7.76	-1
2	2632	0727771101	1879	2.83	39	7.86	-2
2	2726	0727771301	1336	2.64	92	8.09	7
3	277	0136550101	3268	2.14	87	8.45	-1
3	370	0112770101	3862	2.07	6	7.38	1
3	373	0112770201	3723	2.01	6	7.36	1
3	472	0112770601	2932	2.01	5	7.19	-4
3	563	0112770701	3648	2.17	5	7.29	1
3	563	0136550501	3585	2.21	9	7.50	-1
3	554	0112770801	4400	2.10	5	7.37	1
3	645	0112771001	4507	2.12	6	7.42	-4
3	655	0112770501	3945	2.07	8	7.52	-4
3	655	0159960101	4017	2.06	58	8.37	-1
3	735	0112771101	2983	2.05	9	7.42	0
3	835	0136550801	2477	2.04	63	8.19	-1
3	1023	0136551001	2789	2.03	28	7.89	-1
3	1298	0414190101	3017	1.81	76	8.36	-1
3	1381	0414190301	2516	1.86	32	7.91	-1
3	1465	0414190401	5078	2.06	36	8.26	-1
3	1649	0414190501	3326	1.99	41	8.13	0
3	1837	0414190601	3592	2.04	32	8.06	0

Continued on next page

Continued from previous page

Id	orb	obsid	norm	Γ	t (ks)	$^{10}\log(\text{norm}\times t)$	Δ
3	2015	0414190701	2807	1.97	36	8.01	0
3	2199	0414190801	2520	1.96	44	8.04	0
3	2308	0414191001	2117	2.00	29	7.79	-1
4	278	0111850201	1063	1.88	66	7.85	-1
4	852	0165770101	1292	2.02	65	7.93	-1
4	853	0165770201	1348	2.04	69	7.97	-1
4	938	0212090201	1661	2.07	30	7.70	0
4	1012	0310190101	2498	1.95	46	8.06	-1
4	1015	0310190201	1934	2.03	45	7.94	-1
4	1035	0310190501	1886	2.14	47	7.95	-1

2.3 Data processing

The RGS data were extracted using Version 13.5.0 of SAS and the calibration files. Data were binned on a grid with a step size of 0.01 Å. The standard spectra extracted with SAS were transformed into SPEX format using the auxiliary program *trafo*. The four individual spectra of each observation (RGS1 and RGS2, order 1 and 2) were fitted with a simple power law with Galactic absorption, using the SPEX *hot* model for the absorption. For the absorption a cold plasma was adopted, with $kT = 0.5$ eV and standard Lodders et al. 2009 abundances. For the Galactic hydrogen column densities we took values of 1.24 (PKS 2155-304, Wakker et al. 2011), 1.28 (3C 273, Wakker et al. 2011) and 1.36 (H 1426+428, Murphy et al. 1996), in units of 10^{24} m^{-2}. Fitting was done using C-statistics.

For the RGS data, we get the following average values: average net exposure time 35 ks, C-statistic 3037 for an expected value of 2744±73. Thus the fits are not perfect but very good.

Even though the fits are not always perfect, we translated the best-fit model and data into a fluxed spectrum, by convolving the model spectrum with the RGS spectral line-spread function, and then multiplying this convolved spectrum by the ratio of data / model from the spectral fit. The fluxed spectra obtained this way were almost exactly the same as the fluxed spectra obtained directly with the SAS task *rgsfluxer*.

For the fluxed RGS spectrum, we have selected bands of 1 Å wide and determined the average flux in those bands. This is not trivial, because some wavelength bands may have missing data points, e.g. due to hot pixels, CCD gaps etc. Combined with generally positive or negative spectral slopes over the bands, this might give bias. Therefore within each 1 Å wide band, we used our fits with SPEX, then binned the data and model within SPEX to 1 Å wide bins, and multiplied the bin-integrated model spectrum by the ratio of observed count rate to predicted count rate for the same bin.

3 Scattering: the response at short wavelength

We have first briefly investigated the response at short wavelength. To that aim, we have simulated RGS2 spectra for power law spectra. RGS2 is most suitable here because of the presence of CCD7. Initially we have taken bins of 1 Å wide (grid between 4–39 Å) and have determined how many of the counts in each bin are due to photons from the bin itself or its neighbouring bins. The results are shown in Fig. 1.

We see that even for the hardest spectrum, the scattering from distant bins at long wavelength is at most a few percent, and hence small calibration errors are not very important here. However, scattering matters at short wavelength. For the 6–7 Å bin, 25–30% of all counts are from photons with wavelength $\lambda > 7$ Å. To illustrate this further, we have chose a finer bin size of 0.2 Å and repeated this exercise. See Fig. 2. We see a rather discontinuous jump of the fraction of photons from higher wavelength around 7 Å. Between 5.4–5.6 Å, almost 40% of all counts are from photons of 2 bins higher or more, i.e. from $\lambda > 6.0$ Å. Thus, a 10% error in the response for 6 Å photons seen as counts at 5.5 Å would give a 4% error on the measured number of counts in this bin. The effect is the strongest for soft spectra, but even for the hard spectrum ($\Gamma = 0$) the effect is very strong.

Overall, we do not expect a very strong dependence of any residual calibration problems at short wavelengths on the global spectral shape.

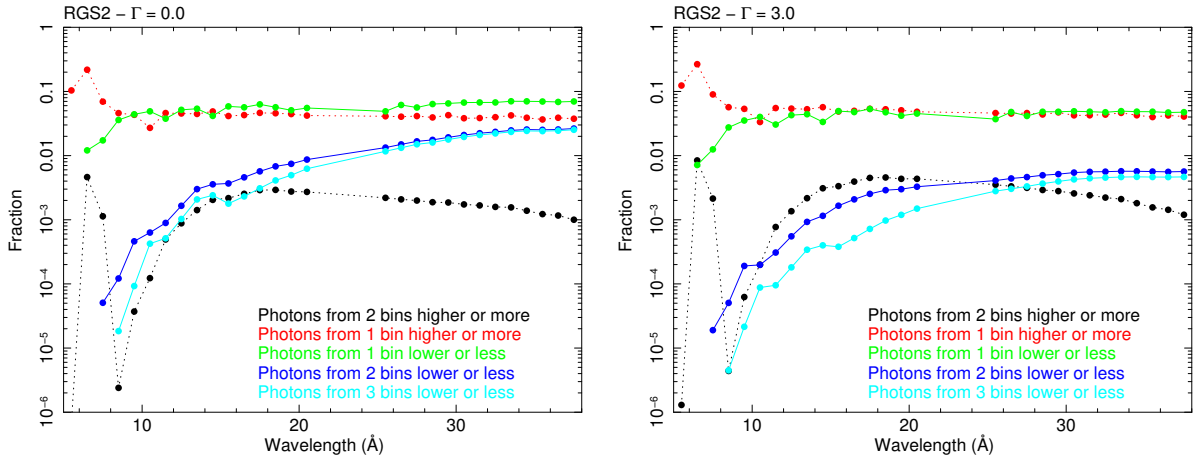

Figure 1: Fraction of all counts in 1 Å wide bins that originate from photons in neighbouring bins, for RGS2 and pure power law spectra with photon indices $\Gamma = 0$ and $\Gamma = 3$.

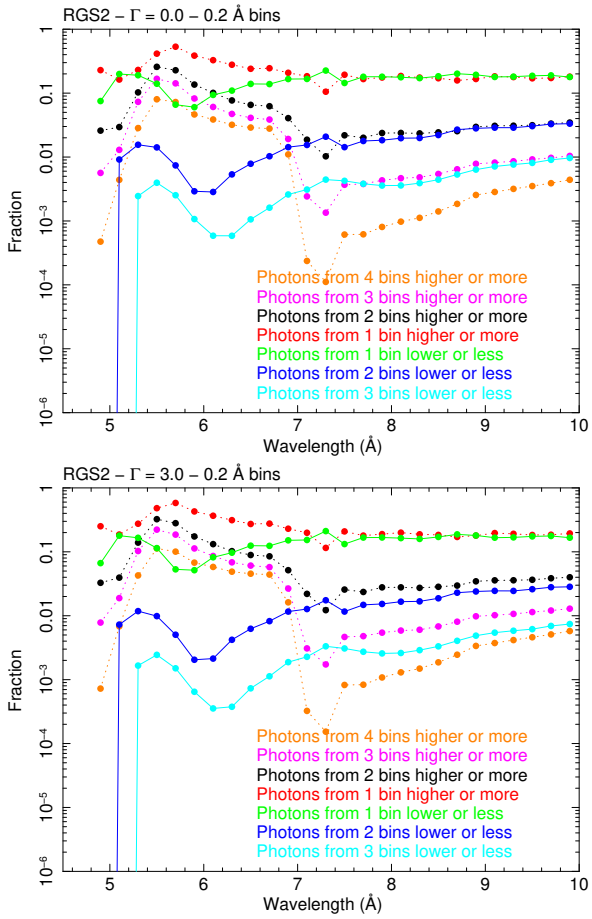

Figure 2: Fraction of all counts in 1 Å wide bins that originate from photons in neighbouring bins, for RGS2 and pure power law spectra with photon indices $\Gamma = 0$ and $\Gamma = 3$.

4 A higher resolution look to the RGS calibration: better models

4.1 Introduction

For a finer look to the calibration, we now switch to narrower bins that are 0.05 Å wide. We also separate the spectra in pieces where RGS1 and RGS2 observe with different CCDs. This is because we stack data taken with different offsets in the dispersion direction, and we want to separate out effects due to the CCD and effects due to the wavelength/energy of the photon.

4.2 Improvements in the spectral models: Galactic absorption

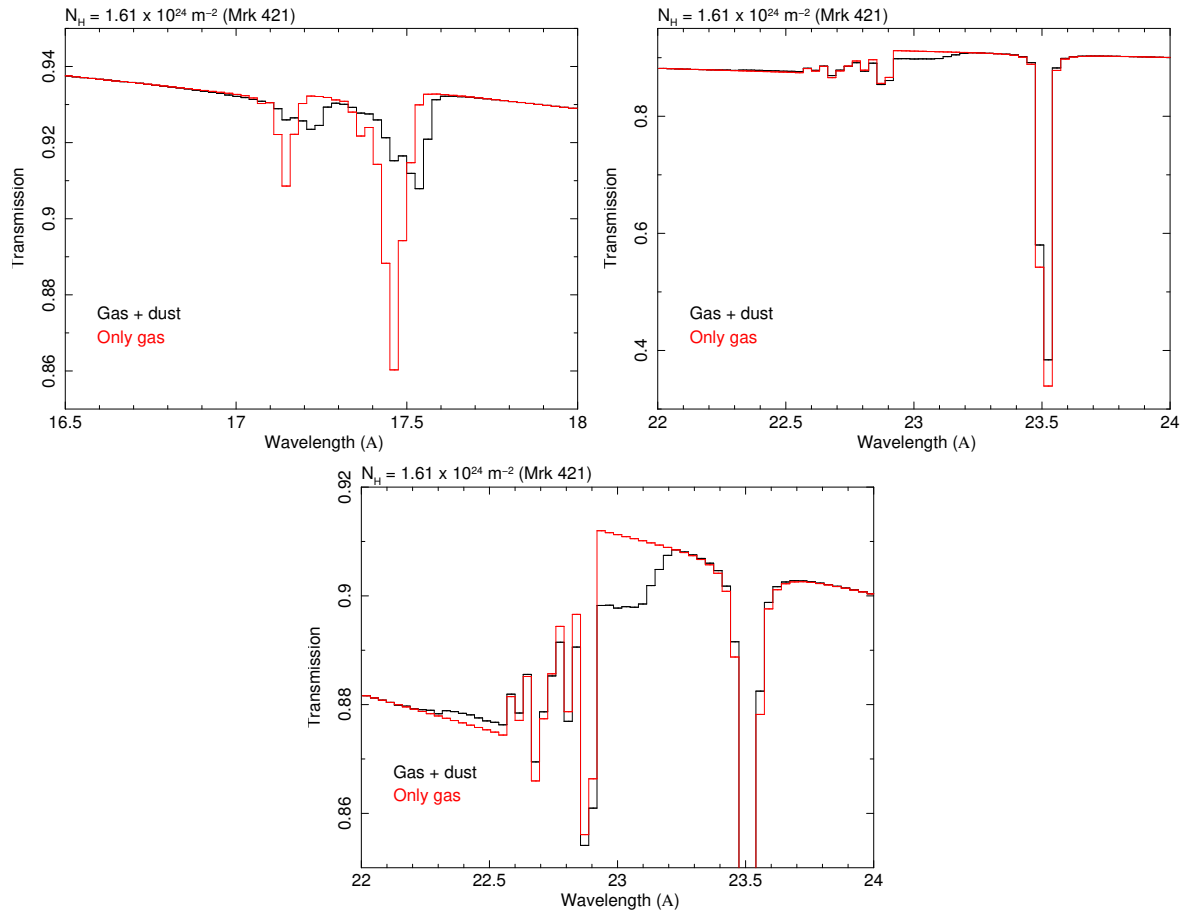

Figure 3: Comparison of the cold interstellar transmission for a model containing only gas, and a gas plus dust mixture.

Up to now, we have used only spectral models with a simple power-law and cold Galactic absorption. However, the ISM also contains some dust, and this can give small changes in the transmission, for the RGS in particular near the Fe-L and O-K edge. We account for this as follows.

From Pinto et al. (2013, A&A 551, A25), from the analysis of 8 X-ray binaries (excluding here SAX J1808.4), we find for oxygen that there is a median of 78% in neutral gas, 5–6% in O II and O III, and 1% in O VI – O VIII. The median dust fraction is 14–15% for oxygen.

From these numbers, we deduce a typical dust to atomic (O I) number ratio of 16%. Costantini et al. (2012, A&A 539, A32) find for 4U 1820–30 that the dust to total oxygen ratio is 20±2%, so not too far off from the median

number we derive from Pinto et al. Costantini find that $MgSiO_3$ gives the best match for the oxygen edge. For the Fe-edge, 87% of pure metallic iron gave the best fit.

Using this, we use the SPEX *amol* model combined with the *hot* model to adjust the cold ISM model. To account fo the depletion, we set the abundances of O, Mg, Si, and Fe to 0.840, 0.187, 0.162 and 0.130 times the standard Lodders et al. proto-solar abundances, and take the column densities of $MgSiO_3$ (SPEX code 3103) and metallic iron (SPEX code 126) to be 3.2285×10^{-5} and 2.8413×10^{-5} times the Galactic neutral hydrogen density.

The differences near the O-K edge are about 1.5% between 22.9 and 23.2 Å, and smaller in other nearby regions; in the O I 1s-2p line at 23.5 Å it als can make a difference of several percent, as well as near 17.45 Å in the Fe-L band (see Fig. 3).

Finally, we note that there can also be weak lines due to the hot, ionised gas of the ISM. We do not model this separately here, but when it comes to determining the effective area corrections we exclude these lines. See Table 2. However, when we look for changes in the effective area as a function of time, these ranges can be used.

Table 2: Ranges possibly contaminated by lines from hot phases of the interstellar medium and excluded from deriving effective area corrections.

$\lambda_{\rm min}$ (Å)	$\lambda_{\rm max}$ (Å)	Transition
12.10	12.15	Ne X
13.40	13.50	Ne IX
15.00	15.05	Fe XVII
16.50	16.60	Fe IX
17.35	17.40	O VII 1s–5p
17.75	17.80	O VII 1s–4p
18.60	18.70	O VII 1s–3p
18.90	19.00	O VIII
21.55	21.65	O VII 1s–2p
22.00	22.05	O VI 1s–2p
23.30	23.40	O II 1s–2p
23.45	23.55	O I 1s–2p
24.75	24.80	N VII 1s–2p
28.45	28.50	C VI 1s–3p
28.75	28.85	N VI 1s–2p
33.40	33.45	C V 1s–3p
33.70	33.80	C VI 1s–2p
34.95	35.00	C V 1s–3p

4.3 Improvements in the spectral models: spectral curvature

It is known that blazar spectra can show spectral curvature. This may affect our models of the intrinsic continua, for which we have used pure power-law spectra up to now. Unfortunately, it is not well possible to use the pn data for this due to uncertainties in its calibration around and below the oxygen edge ($E < 0.5$ keV).

In principle, the power-law model of SPEX has additional parameters that can be used to introduce a spectral curvature, namely a break energy, a photon index break and a smoothing parameter for that. See the SPEX manual for more details. Unfortunately, in practice this cannot be used for automatically fitting a large number of spectra. The main reason is that sometimes the break can be near the lower or upper boundary of the RGS spectrum, in which case some parameters become poorly determined or start strongly correlating.

Therefore we follow another approach. SPEX also has the *knak* multiplicative component. This uses piecewise power-law functions that are multiplied by the underlying continuum. Free parameters are the wavelengths w_i of the knots of this function, as well as their values f_i at w_i.

We first fit the spectrum with a pure power-law with cold absorption, and then freeze the normalisation and photon index of this power-law. Then we add the *knak* component with 3 knots, with the first and last one fixed ($w_1 = 7$ Å, $w_3 = 38$ Å), and the middle wavelength w_2 a free parameter (forced to be between w_1 and w_2). In addition, the three normalisations f_1 to f_3 are free parameters.

We do an initial grid search over w_2 to find a good starting value, and then do a full fit.

For the data, we do a full fit to the combined RGS1 and RGS2 first order spectra. In addition, we take the relative normalisation of RGS2 relative to RGS1 as a free parameter.

4.4 Results of the new fits

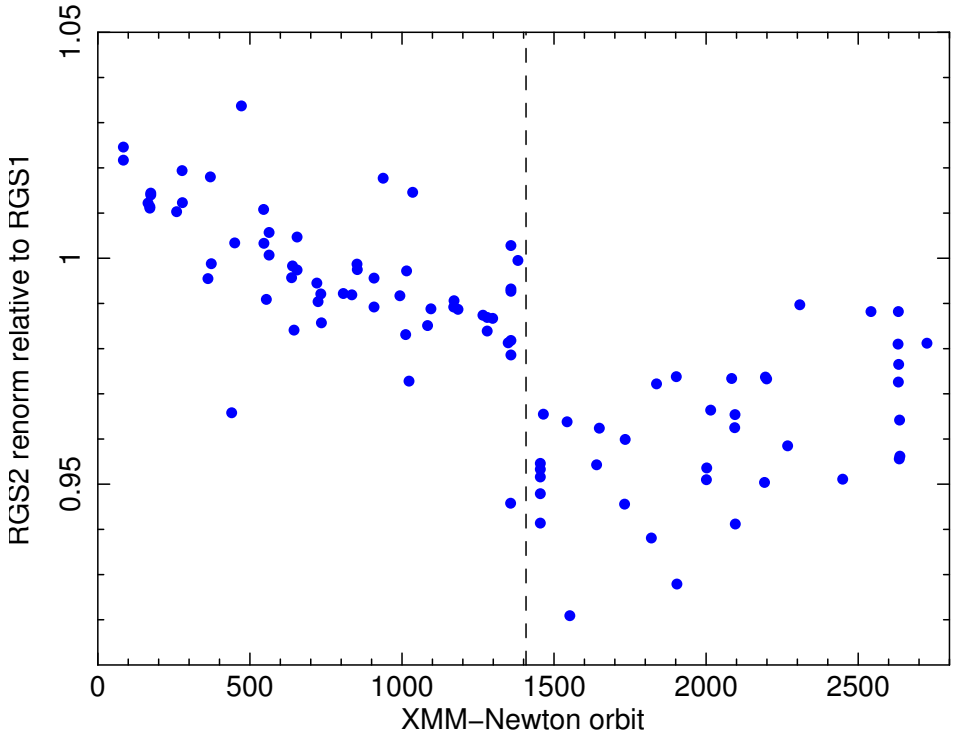

Figure 4: Relative normalisation of RGS2 relative to RGS1 for the new fits to the combined RGS1 and RGS2 first order spectra.

Some important results of our new fits are shown in Fig. 4 and Fig. 5. The first figure shows a strong linear decrease in the renormalisation from about 1.02 to 0.98 during the first 1400 orbits of the mission. Around orbit 1408, where RGS2 started the single-node readout, an additional drop by about 3% occurred. Since then, the renormalisation is slowly rising again but with a large scatter. This confirms our earlier conclusions that while – on average – RGS1 is stable when compared to pn, RGS2 is not. Of course, there can be wavelength-dependent effects that will be investigated as a next step.

A possible scenario for what could happen around orbit 1408 is that there is a small but sudden jump in the QE for the CCDs with lower energies (for these the dependency on threshold settings is larger) and this could be at the level of 1-3% (eventually wavelength dependent as onboard thresholds are set per half CCD and ground cuts are probably a function of wavelength (first order only).

From Fig. 5 it follows that 3C 273 is not a suitable target for our purposes: it always has a spectral break around 13–20 Å, in the sense that it has a soft excess. Furthermore, the observations of H 1426+428 have relatively poor statistics, and hence we will ignore them further, focussing solely upon Mrk 421 and PKS 2155-304.

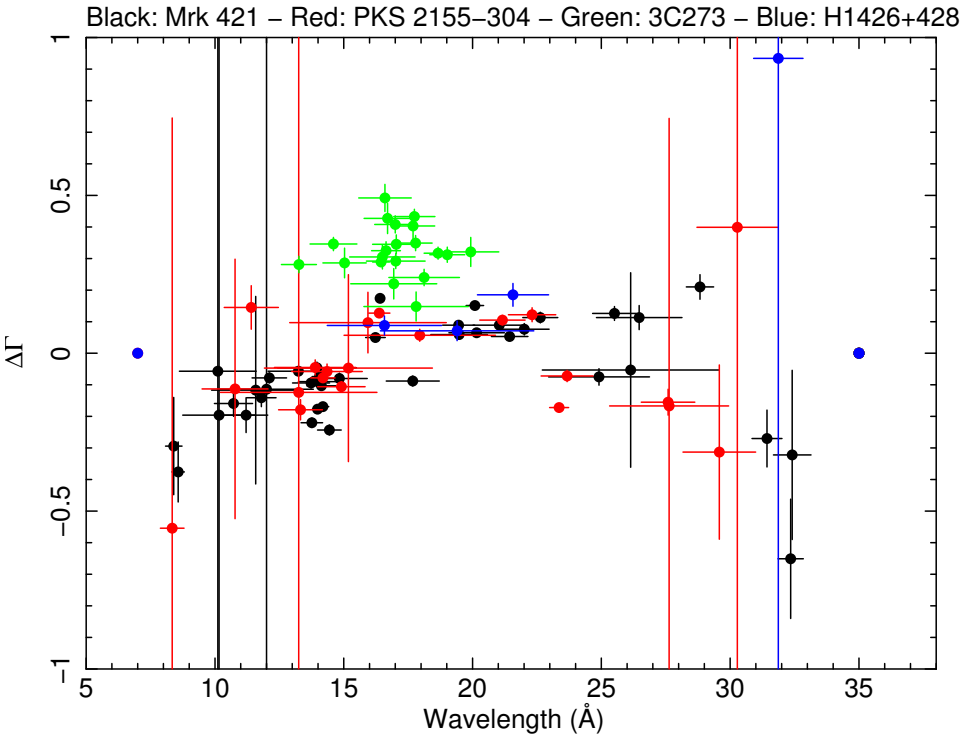

Figure 5: Break in photon index versus break wavelength for the observations used in this study. A negative break means softening of the spectrum towards higher energies (shorter wavelengths). Note that there are also several observations that show no significant break; these are collapsed in the endpoints at $\Delta\Gamma = 0$ and 7 or 35 Å.

5 Deriving the effective area corrections for RGS1 and RGS2

5.1 Method

We are now in the situation to derive the effective area corrections for RGS1 and RGS2. Our procedure is as follows.

For each 0.05 Å wide bin, we determine the fit residuals for each individual observation relative to the best-fit broken power-law model described in the previous section. We then fit these residuals as a function of time to a simple analytical expression. This is done for first and second order spectra independently.

It the observation epoch is denoted by t, expressed in units of 1000 orbits, then we use the following parameterisation:

- $t < 0.538$: $f = p_1 + (t/0.538)p_2$
- $0.538 < t < 1.408$: $f = p_1 + p_2 + p_6 + ((t - 0.538)/0.870)p_3$
- $1.408 < t < 2.112$: $f = p_1 + p_2 + p_3 + p_6 + p_7 + ((t - 1.408)/0.704)p_4$
- $2.112 < t < 2.816$: $f = p_1 + p_2 + p_3 + p_4 + p_6 + p_7 + ((t - 2.112)/0.704)p_5$

The reasoning behind this parameterisation is as follows. Around orbit 538 both RGS detectors were cooled, thus their performance may have changed discontinuously. The parameter p_6 accounts for such possible discontinuities. Similarly, around orbit 1408 RGS2 went into single-node readout mode, also causing possible discontinuities (see Fig. 4). The corresponding jump is represented by p_7. The parameter p_1 represents the initial calibration mismatch at the start of the mission. Further, the parameters p_2 – p_5 represent the integrated gradual changes in the intervals 0 – 0.538, 0.538 – 1.408, 1.408 – 2.112 and 2.112 – 2.816. The times 2.112 and 2.816 have no particular meaning, but are convenient as they are exactly 1.5 and 2 times the critical time 1.408.

We have fitted the residuals now to the above form. In our first fit, we have all 7 parameters free; we then fit p_7 to a simple spline in λ, with a typical spacing of 1 Å for first order spectra and 0.5 Å for second order spectra (note that for the second order spectra we use the model derived from the first-order spectra).

In general we use this spline spacing, except for p_1 for which we use 0.2 or 0.1 Å for first and second order spectra, respectively. In a few exceptional cases we had to add a relatively narrow Gaussian to the spline in order to represent the derived parameters p_i properly.

5.2 Results

We have created tables for both RGS detectors and both spectral orders, giving for a resolution of 0.01 Å the parameters $p_1 - p_7$ and the corresponding CCD for which the fit is valid. We also have a simple fortran subroutine that calculates as a function of wavelength and XMM-Newton orbit number the correction factor to the effective area.

Furthermore, we show our fits to the parameters in the figures at the end of this paper (Fig. 16–45).

5.3 Quality of the correction factors

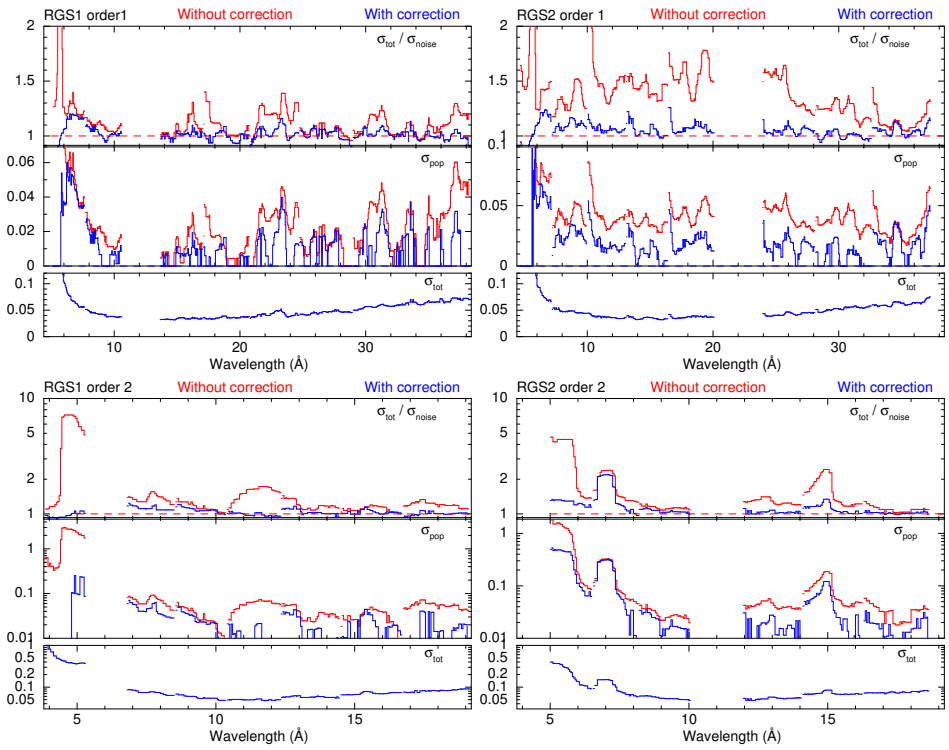

Figure 6: Comparison of residuals. See text for more explanation.

We have checked the quality of our new calibration as follows. We have taken all spectra of Mrk 421 and PKS 2155, and have determined the residuals to the individual broken power law fits discussed before. We have done this for the spectra without the new calibration, and with the new correction. The residuals are caused by both the statistical noise ($\sigma_{\rm noise}$, the Poissonian measurement errors) and the rms variations due to the remaining systematic calibration uncertainties (dubbed here $\sigma_{\rm pop}$). Obviously, we have for the total variance

$$\sigma^2_{\rm tot} = \sigma^2_{\rm noise} + \sigma^2_{\rm pop}. \qquad (1)$$

We measure $\sigma_{\rm noise}$ and $\sigma_{\rm tot}$, and get $\sigma_{\rm pop}$ through Eq. 1. Due to statistical fluctuations, this quantity can become formally imaginary (when $\sigma^2_{\rm pop} < 0$. In those cases we put it to zero.

We show our results for both RGS detectors and both spectral orders in Fig. 6. We can draw a few conclusions from these figures.

- For most wavelengths, the new calibration provides substantially better results, as seen in the upper panel for each configuration: the total variance is close to the variance of the measurements.
- The middle panels show that for RGS1 in first order for most wavelengths the remaining systematic uncertainties are less than 1%; for RGS2 this is 2%.
- There are some regions with notably higher residuals: below 9 Å increasing up to 5%, near the neutral oxygen edge (23 Å) and near the nitrogen edge (31 Å).
- For the second order spectra the remaining residuals are somewhat larger, but note that these are in general much smaller than the effective area corrections that we derive. From an inspection of the fit residuals of the parameter p_1 we see how large these correction factors can be. In fat, we have substantially improved the second order calibration.

5.4 Some sanity checks

We have checked quickly how the new calibration works on our targets. It works very well, and some examples are shown in Fig. 7.

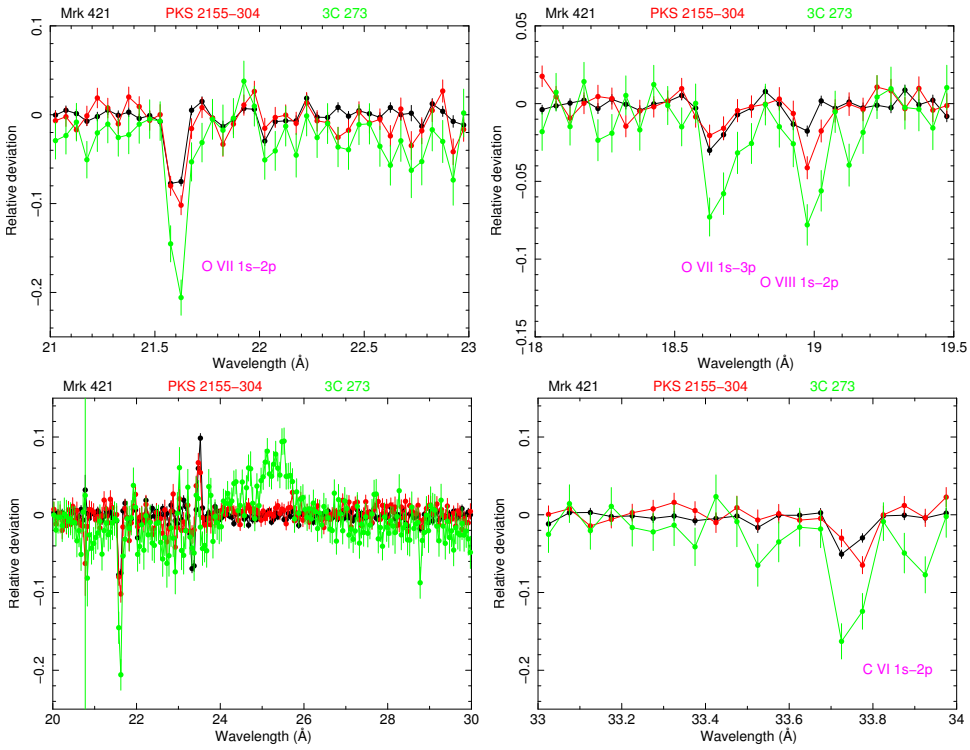

Figure 7: Stacked residuals of the combined RGS1 and RGS, order 1 and order 2 spectra of Mrk 421, PKS 2155-304, and 3C 273. We show a few of the astrophysical lines of hot, ionised gas (that were taken out in deriving the effective area corrections). Outside these lines, the residuals are very small, less than 1% over most of the range for the "perfect" broken power-laws Mrk 421 and PKS 2155-304. Note that 3C 273 does not have such a simple continuum shape and in addition contains weak absorption features intrinsic to the source. In general, we can see the different ISM columns towards these three sources by comparing the depths of the absorption lines.

6 Some possible physical effects

6.1 Near the oxygen edge

It is interesting to look to the effective area corrections near the oxygen edge. This is best seen in Fig. 19, lower panel. It looks like there is apparently still a jump of 3–5% near 23 Å in the effective area that was not taken into account. This observed jump is of the same order as the Galactic foreground O I edge in these sources (see Fig. 3). For this analysis we use the more modern Lodders et al. (2009) proto-solar abundances for the ISM; the older value for the oxygen abundance that was used in the earlier work on the instrumental oxygen edge by De Vries et al. (2003) was the one by Wilms et al. (2000), which was 19% smaller than the present value. However, such an effect works in the opposite direction. Adopting the newer abundances that correspond to a higher interstellar O-edge implies that the instrumental oxygen edge should be *less deep*, by 0.9% or 0.7% for Mrk 421 and PKS 2155-304, respectively. Here we used that the oxygen edge for Lodders abundances is 2.9% per 10^{24} m^{-2} hydrogen column density. Thus, most likely the feature seen in Fig. 19 is more a gradual change, not associated with the oxygen edge, than an edge.

6.2 Hydrazine contamination?

For RGS1 CCD2 we see some strong features in the effective area near 31 Å (see Fig. 17). We see that a part (but not all of it) is apparently time variable. First, there is a dip near 31.1 Å for parameter p_2. This represents the discontinuity at the time of cooling of the RGS detectors. The negative peak of about 10% amplitude indicates here that the observed has lowered by that amount. Looking to p_1, there was indeed a positive peak of order 10% at that wavelength. Apparently, some "hot" pixels at that wavelengths causes some excess counts, and these have disappeared after cooling.

But there is more in this band. In p_1, we also see a peak at 30.7 Å of about 10% that gradually disappears during the first 534 orbits (as evidenced by the negative peak at that wavelength of parameter p_2 that represents the change between orbit 0 and orbit 534).

Accounting for this, there still remains a deep and broad trough around 30.6 Å. We have long thought about it, but concluded the following possibility at our April 2015 RGS calibration meeting. The feature is close to the nitrogen edge.

Now hydrazine (N_2H_4) is used a propellant for the thrusters of XMM-Newton. It decomposes into ammonia, NH_3, and N_2 after combustion. Both chemicals contain nitrogen, and when the material is deposited on any part of the light path, it may cause distortion on the effective area, either through altering the transmission or reflection.

We propose that the 30.6 Å feature is a discrete absorption structure due to hydrazine and/or its burning products. It may be either bound to the CCD surface (probably consisting of aluminium oxyde), in which case it affects the transmitted spectrum seen in the RGS, or it may be sticking to the XMM-Newton gold mirrors, in which case it affects the reflectivity; in the latter case, the effect should be seen both in RGS and MOS.

Note that the features is only present in RGS1.

Unfortunately there is not much experimental data available on this. See for instance Fig. 8.

6.2.1 Transmission near the nitrogen edge

We consider here first transmission. This may be the case if the material is deposited e.g. on the CCD's of the RGS. The nitrogen in the compound will give discrete, broadened features near 30 Å in the transmission. The K-shell cross section near the nitrogen edge of molecular nitrogen, ammonia and hydrazine are shown in Fig. 8. Cleary each chemical has its own characteristic absorption structure.

We have attempted to approximate the average fit residuals of the stacked RGS1 spectra, compared to the power-law models, to such a model. The results are shown in Fig. 9. From the depth of the feature, we would need a typical column density of $(4 \pm 1) \times 10^{20}$ molecules m^{-2}. This corresponds to a layer of 21 nm of hydrazine, where we used the mean molecular weight of 32,0452 a.m.u. and density of 1021 kg m^{-3}. Note that the melting and boiling points of hydrazine are 2 and 114 degrees Celsius.

Although such a thickness reproduces the depth of the feature, details differ. First, there is a smooth deviation between 28.5–30 Å visible in the plot; this may have nothing to do with the hydrazine, but may simply be the broad-

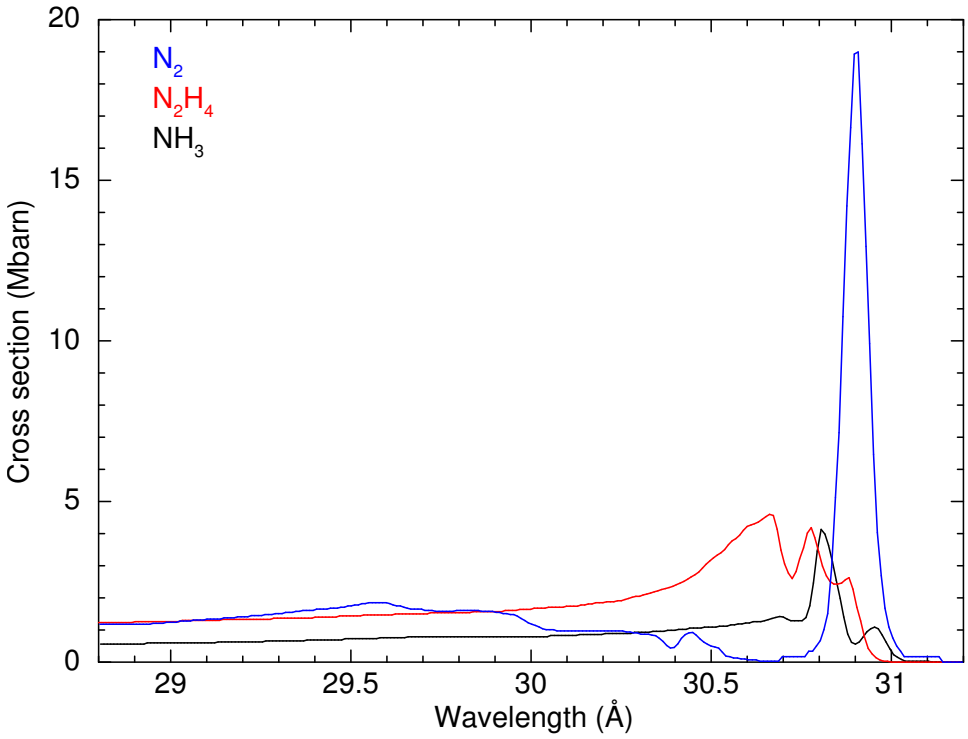

Figure 8: Absorption cross sections for three nitrogen compounds. Data digitised from Figs. 4.3 and 4.4 in J. Stöhr, *NEXAFS Spectroscopy*, Springer, 1992.

band effective area uncertainties of RGS. However, although the depression in the data near 30.6 Å is close to that from Hydrazine, in detail there are differences.

We mention here that the hydrazine, if deposited e.g. on the CCD, may form chemical bonds with the Al surface layer, and this may alter the fine structure. Also, while we focus here on hydrazine, also its nitrogen-containing burning products might bind to the surface and cause modifications in the transmitted spectrum. Whatever form it has, we apparently need a layer of about 21 nm thickness containing a nitrogen-compound to explain the observed fine structure near 30.6 Å.

To ease further identification, the observed structure can be described by the sum of two gaussians, with centroids, σ and equivalent width of 30.97, 0.093 and 0.022 Å for component 1 and 30.49, 0.153 and 0.040 Å for component 2.

6.2.2 Reflection

We next consider the case where hydrazine or its decay products are deposited on the XMM-Newton mirrors. In that case they will affect the reflectivity of the gold layer and therefore modify both the effective area of the MOS detector and the RGS detector.

We have used `http://henke.lbl.gov/optical_constants/bilayer.html` to calculate this case. We take a substrate of Ni, with a 250 nm gold layer deposited on it, and on top of that a layer of hydrazine. The reflection angle that we use is 0.5 degree. These numbers are appropriate for the XMM-Newton mirrors. The reflectivity of this structure, relative to the reflectivity without hydrazine contamination, is shown in Fig. 10.

Note that for the X-ray mirrors we need two reflections, so to get the effect on the effective area, these relative reflectivities need to be squared. The effect is high non-linear as a function of the thickness, but we estimate that to get a jump of 5% in the effective area at the nitrogen edge (a 2.5% jump in the reflectivity), we need a layer of about 55 nm thickness (see also Fig. 11).

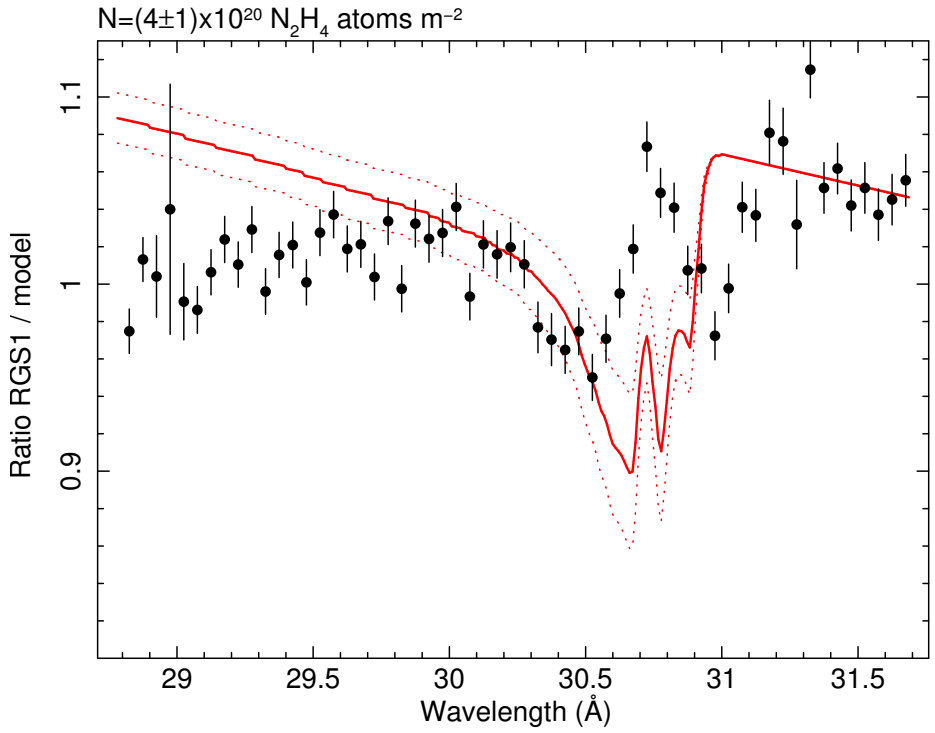

Figure 9: Ratio of the stacked RGS1 spectrum to the best-fit model near the nitrogen edge. The model is a fit by eye with a layer of Hydrazine as indicates in the figure.

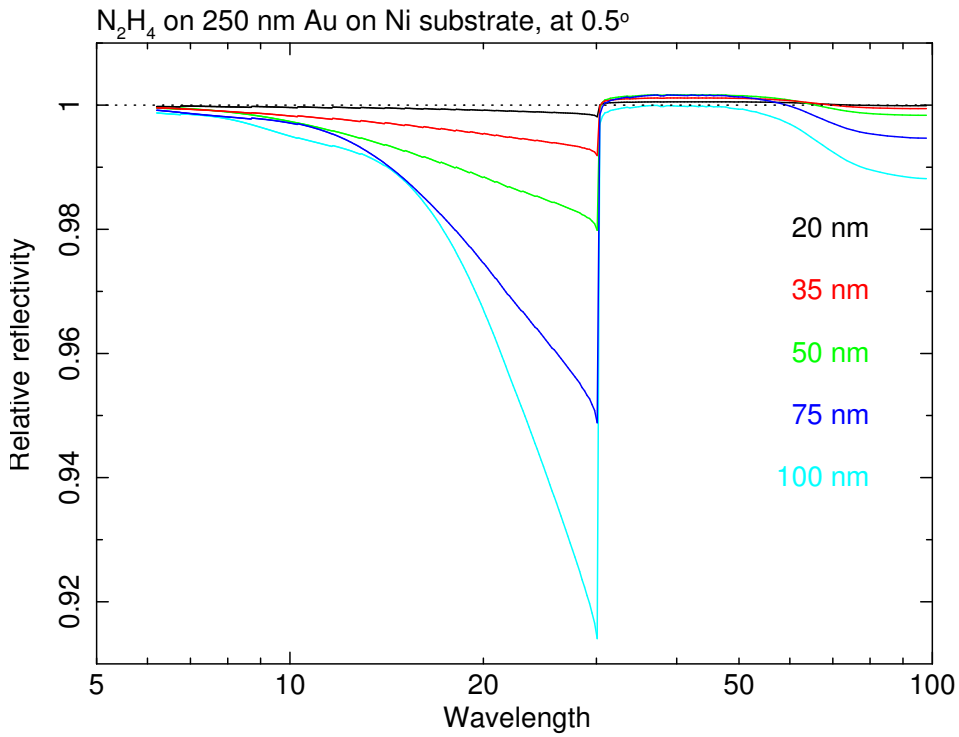

Figure 10: Reflection of a gold layer contaminated by hydrazine, relative to the reflection of a pure gold layer, for different thicknesses of the hydrazine layer.

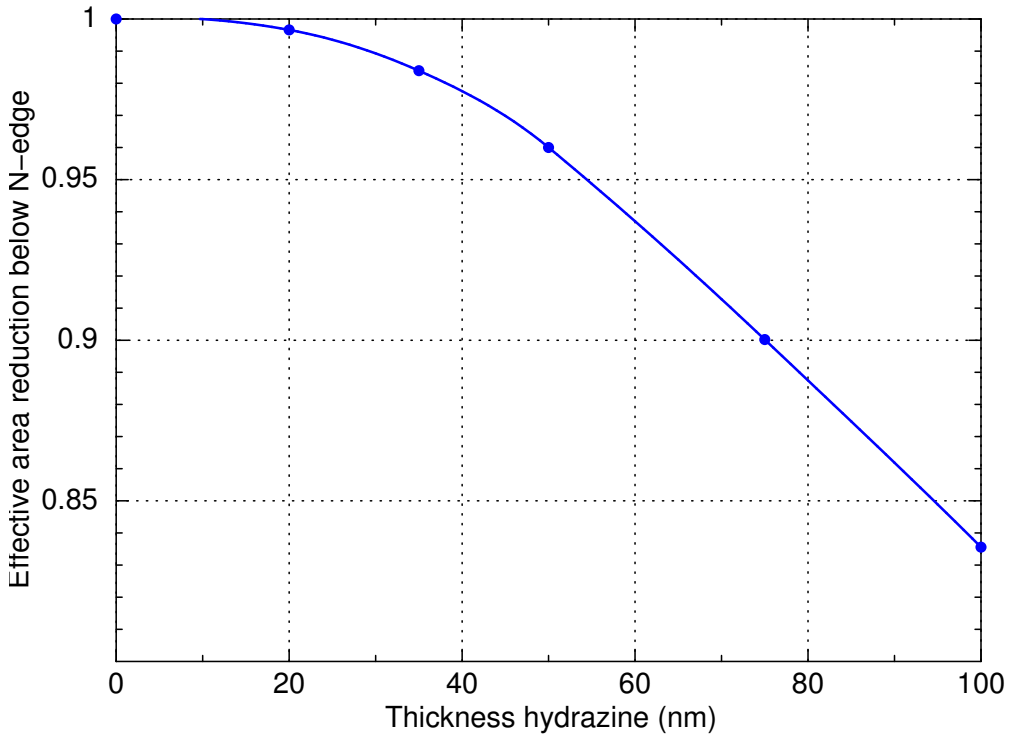

Figure 11: Reduction in the relative effective area of the XMM-Newton mirrors below the nitrogen edge, as a function of the thicknesses of a contaminating hydrazine layer.

7 Conclusions

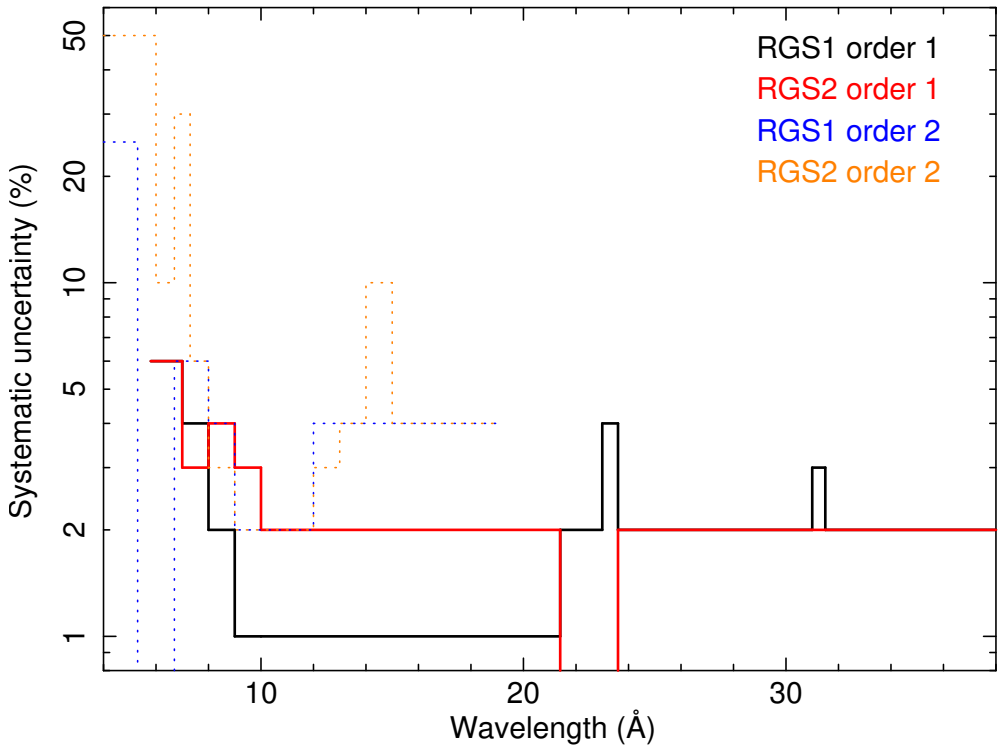

Figure 12: Schematic representation of the present calibration uncertainty of the effective area (conservative limits).

We have obtained a better calibration of the RGS effective area based on empirical modelling. We see some changes near the time of cooling of the RGS detectors, and in particular for RGS2 a strong drop of several percent in the effective area around the time of single-node readout. In general, there appear to be gradual wavelength- or CCD dependent variations in the effective area.

Due to the empirical method that we use, it is not well possible to attribute the derived correction factors to the CCD (pixel) quantum efficiency or to the overall effective area. However, we derived them for each CCD independently, hence to first order they may be linked to position on the CCD. More testing is needed on different sources to see how this calibration affects the derived spectra. We used already the bright blazars for our calibration work, hence one might consider to take an X-ray binary (without pile-up) for further testing.

How accurate is our calibration? See Fig. 6, the blue lines (with correction) in the middle panels ($\sigma_{\rm pop}$). In general, in first order we have an accuracy of 1 or 2% for RGS1 and RGS2, respectively, over most of the band. See Fig. 12 for a schematic overview of the estimated remaining systematic uncertainties.

The effective area shows signatures of nitrogen, possibly related to the rocket fuel that is used to fine-tune the orbit of the satellite.

Finally, for the first time we have obtained a reasonable calibration of the second order spectrum of RGS.

8 Some examples of the correction factors

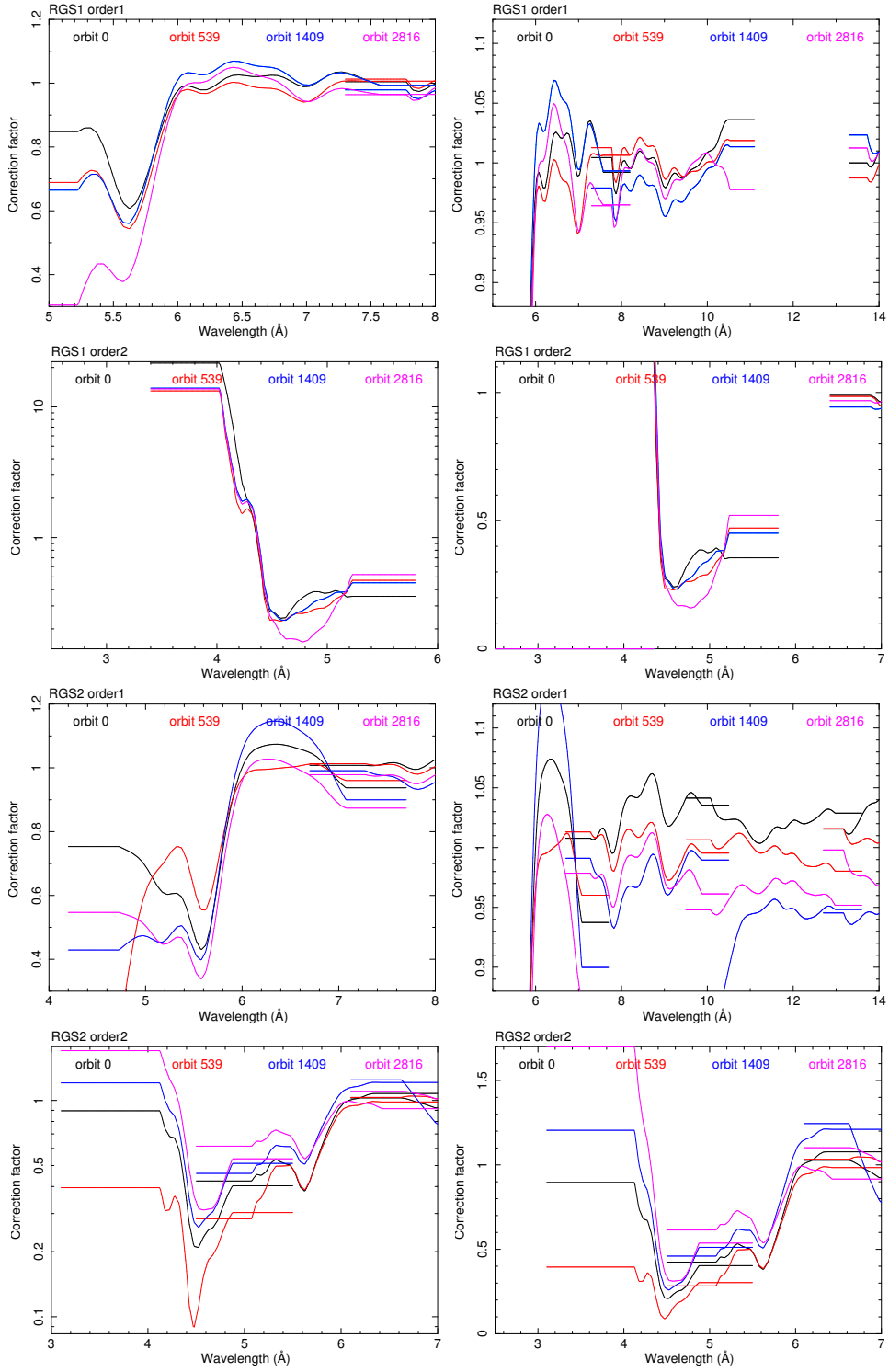

Figure 13: Effective area correction factors at selected epochs

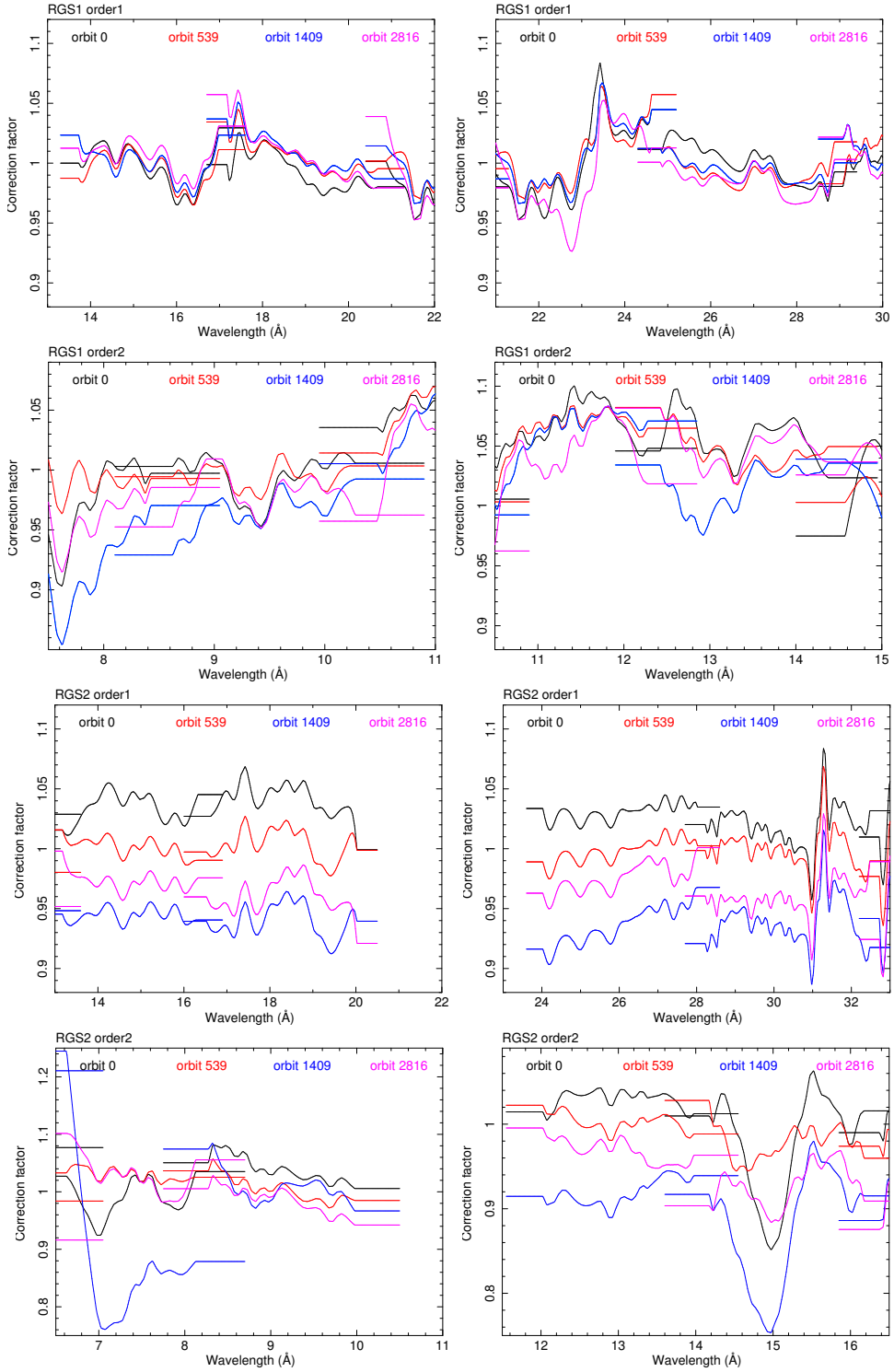

Figure 14: Effective area correction factors at selected epochs

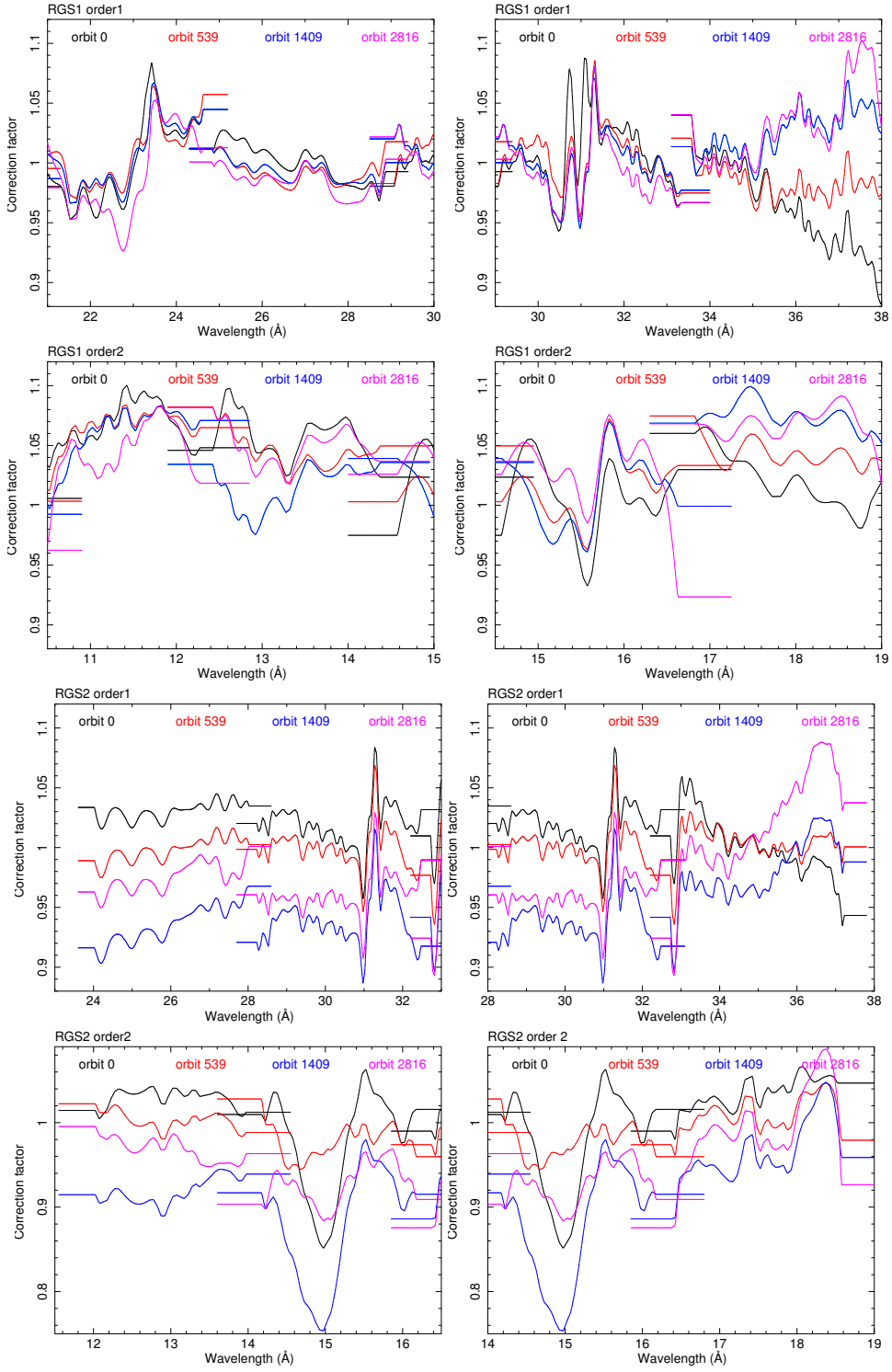

Figure 15: Effective area correction factors at selected epochs

9 Appendix: Plots of fits to the correction parameters

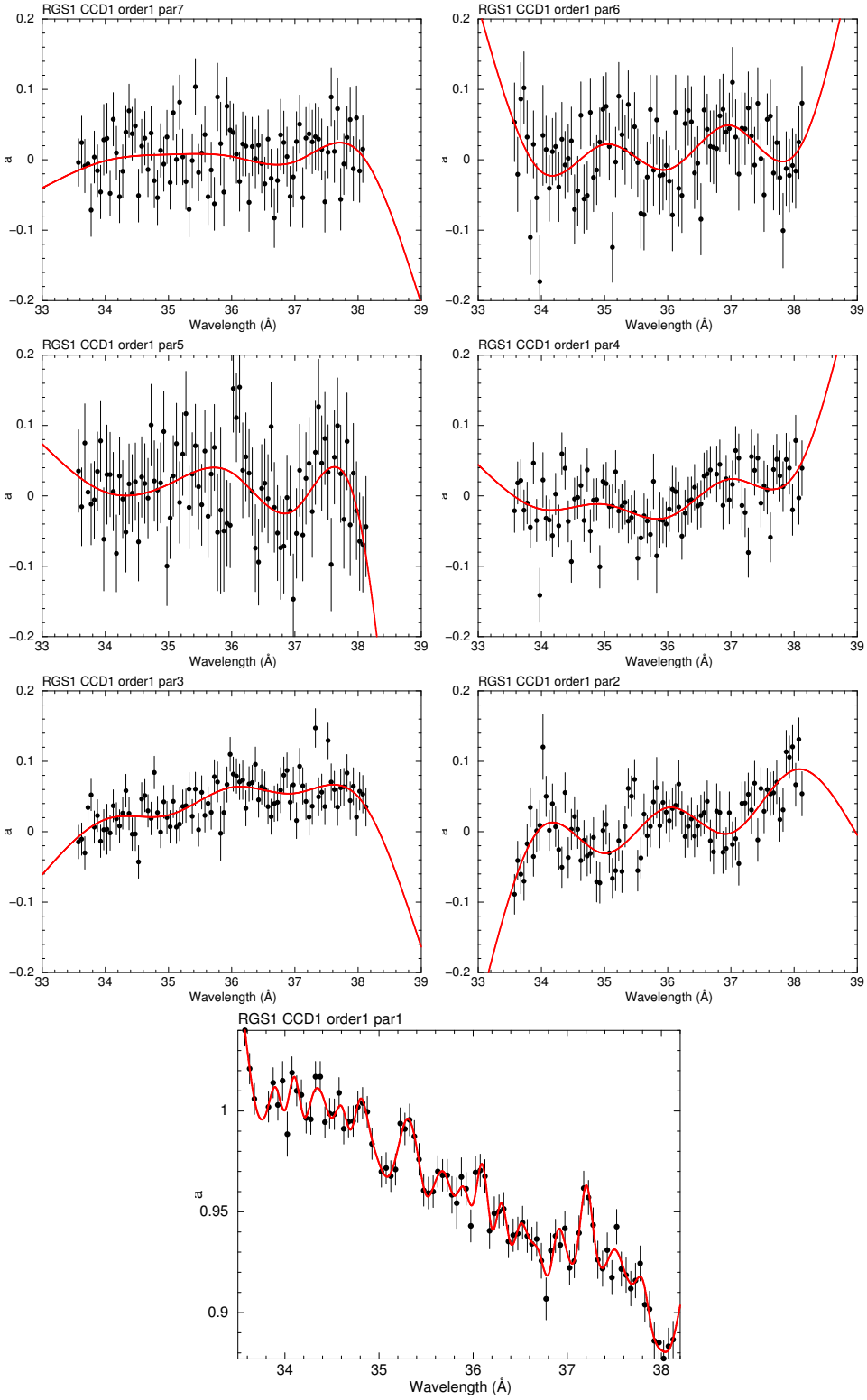

Figure 16: Fits to $p_1 - p_7$ for RGS1, order 1, CCD1

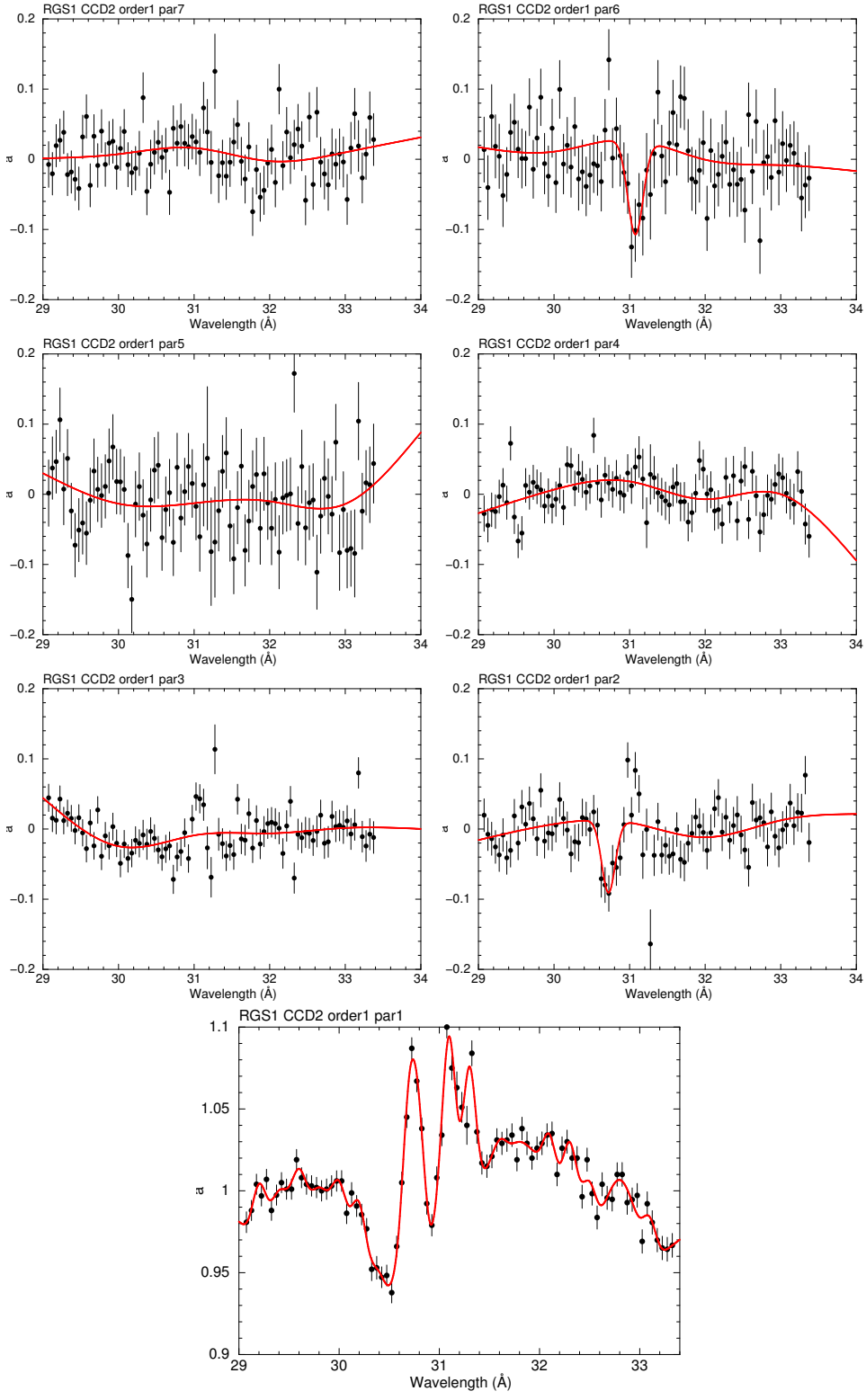

Figure 17: Continuation of previous figure.

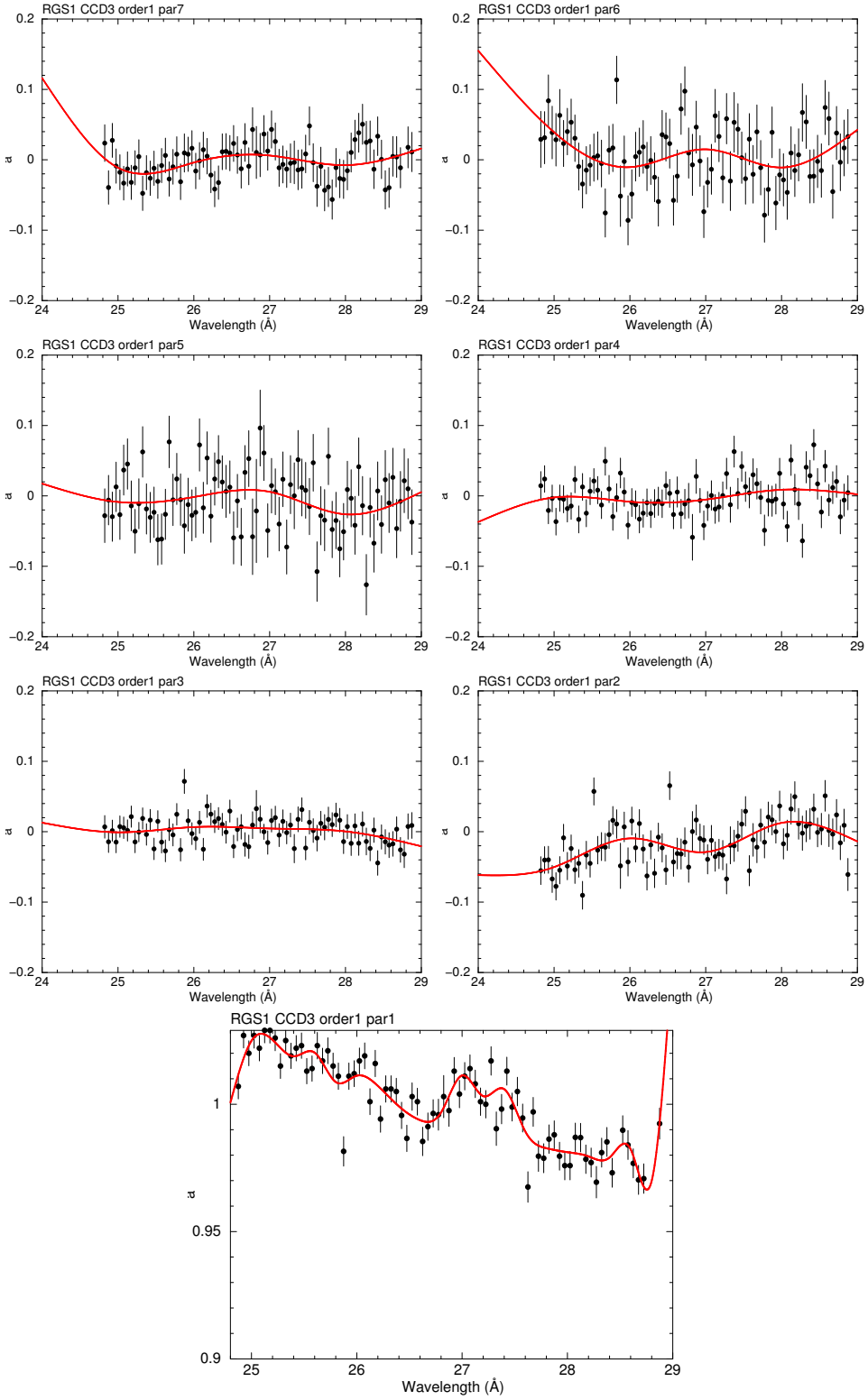

Figure 18: Continuation of previous figure.

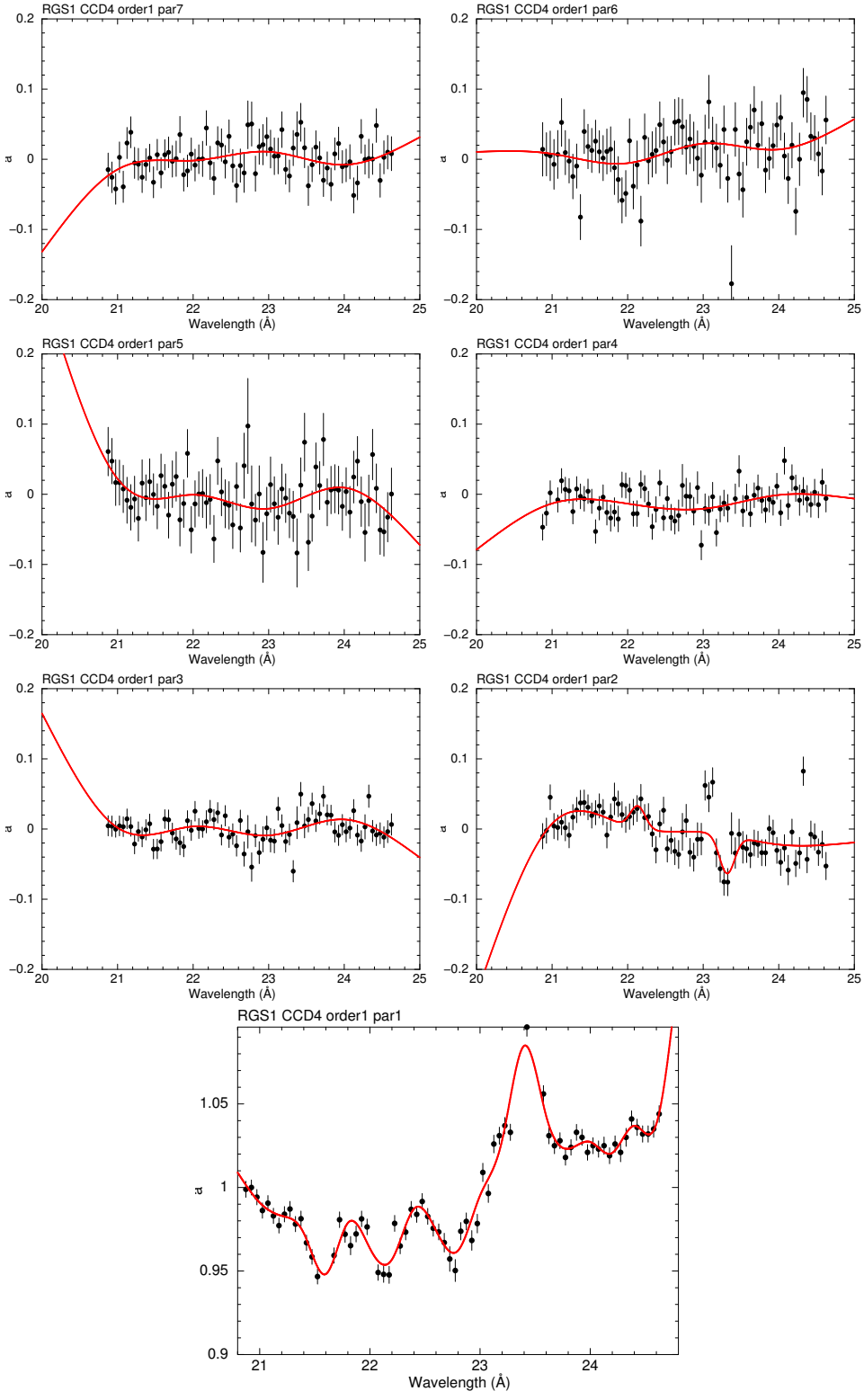

Figure 19: Continuation of previous figure.

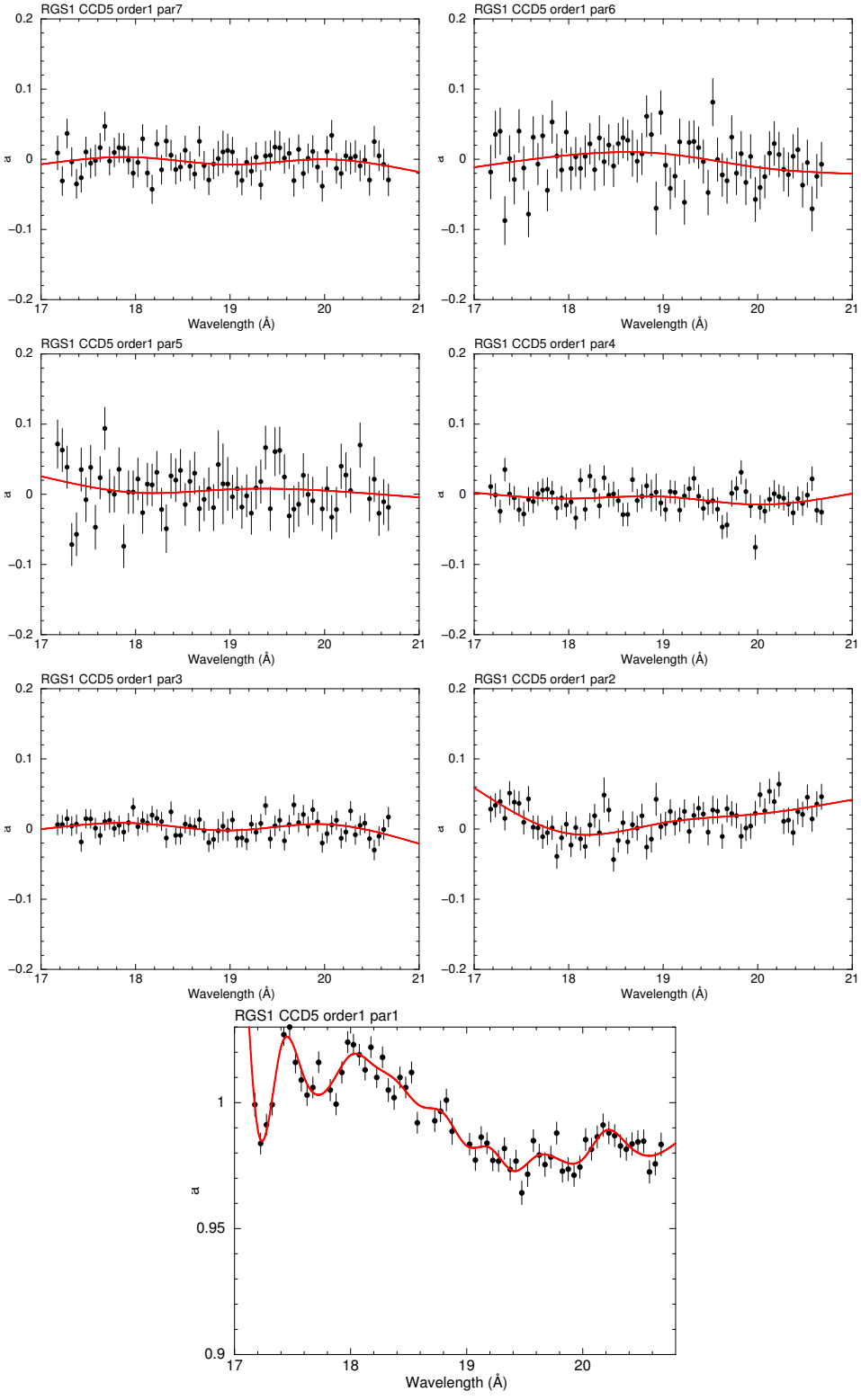

Figure 20: Continuation of previous figure.

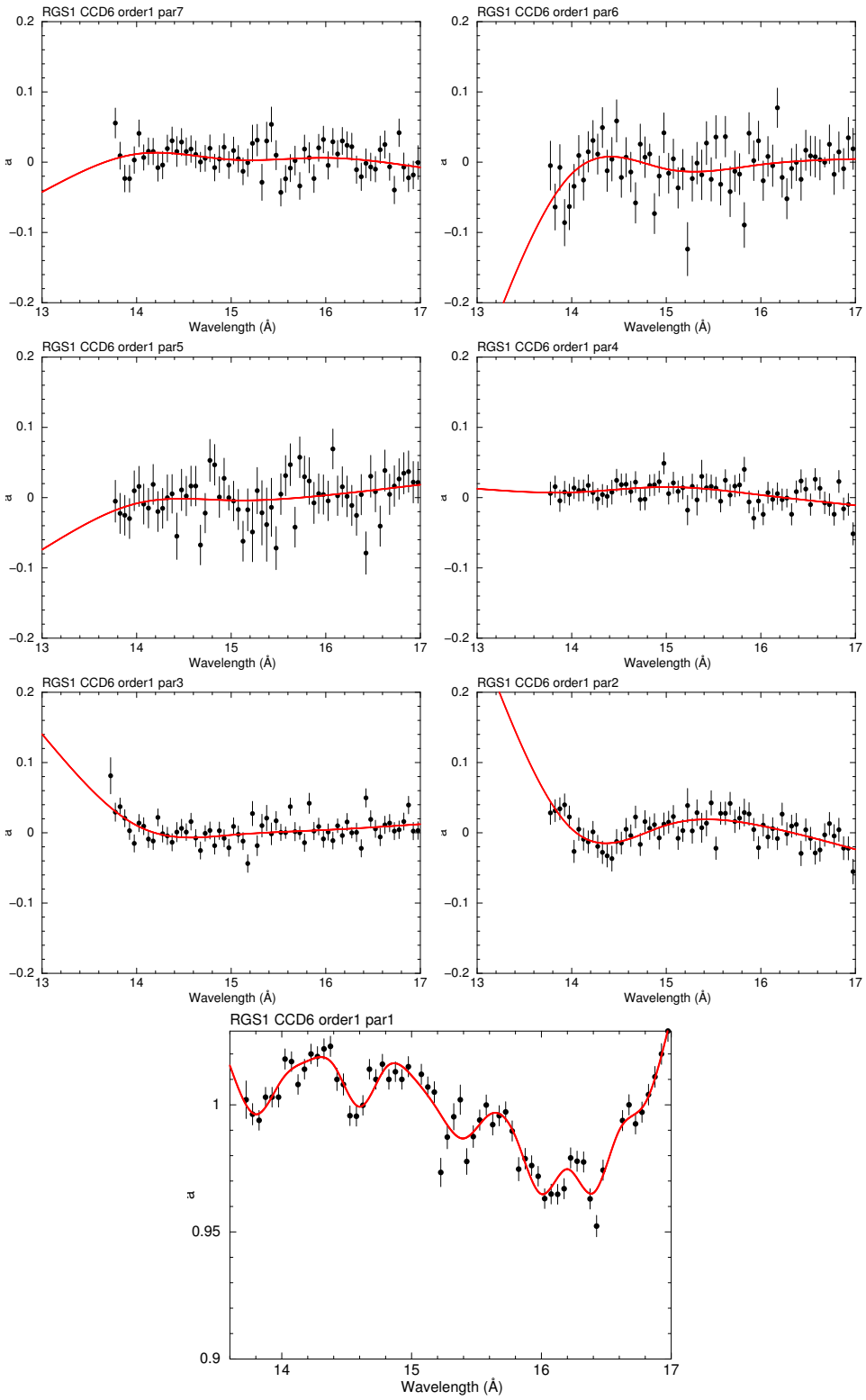

Figure 21: Continuation of previous figure.

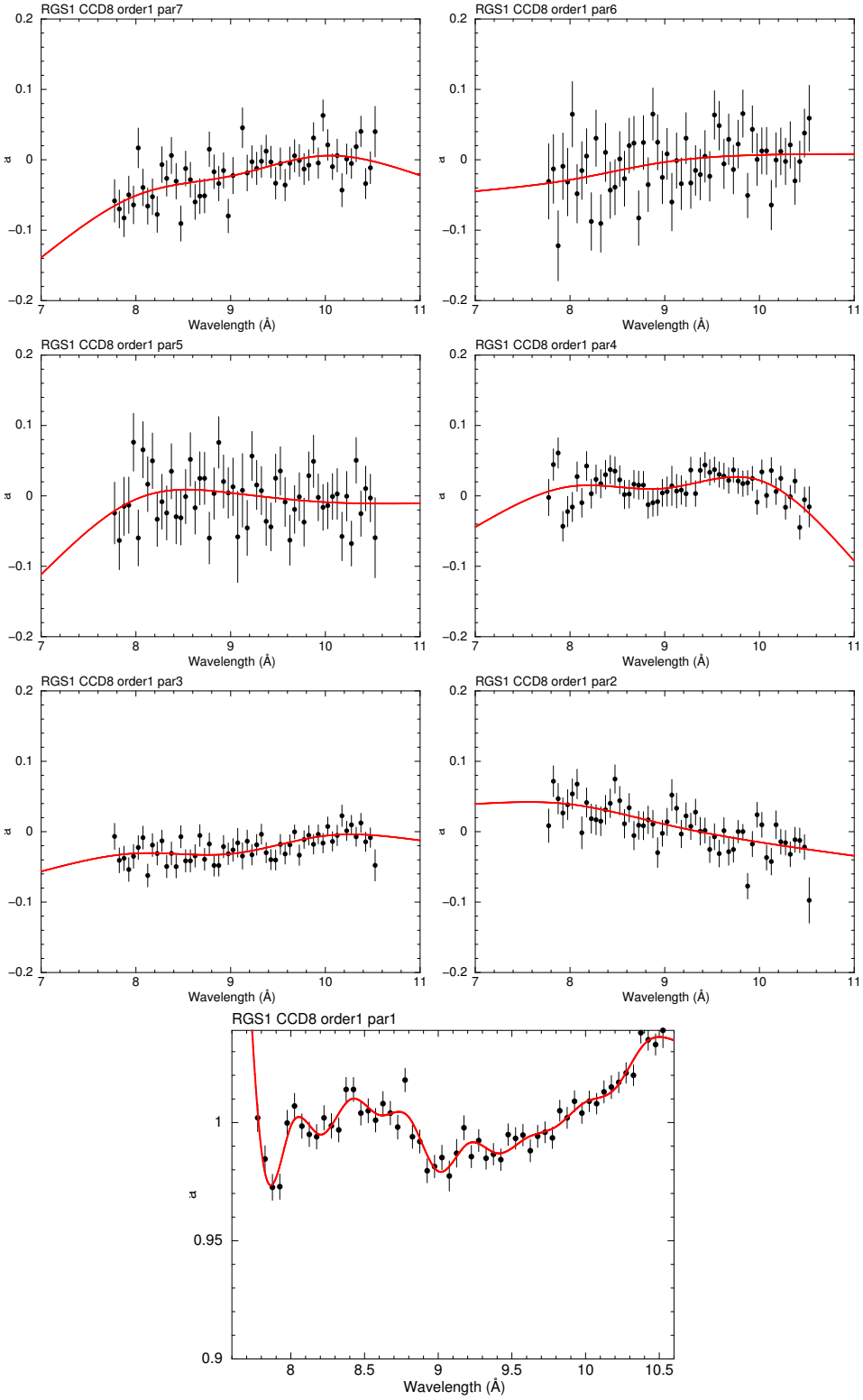

Figure 22: Continuation of previous figure.

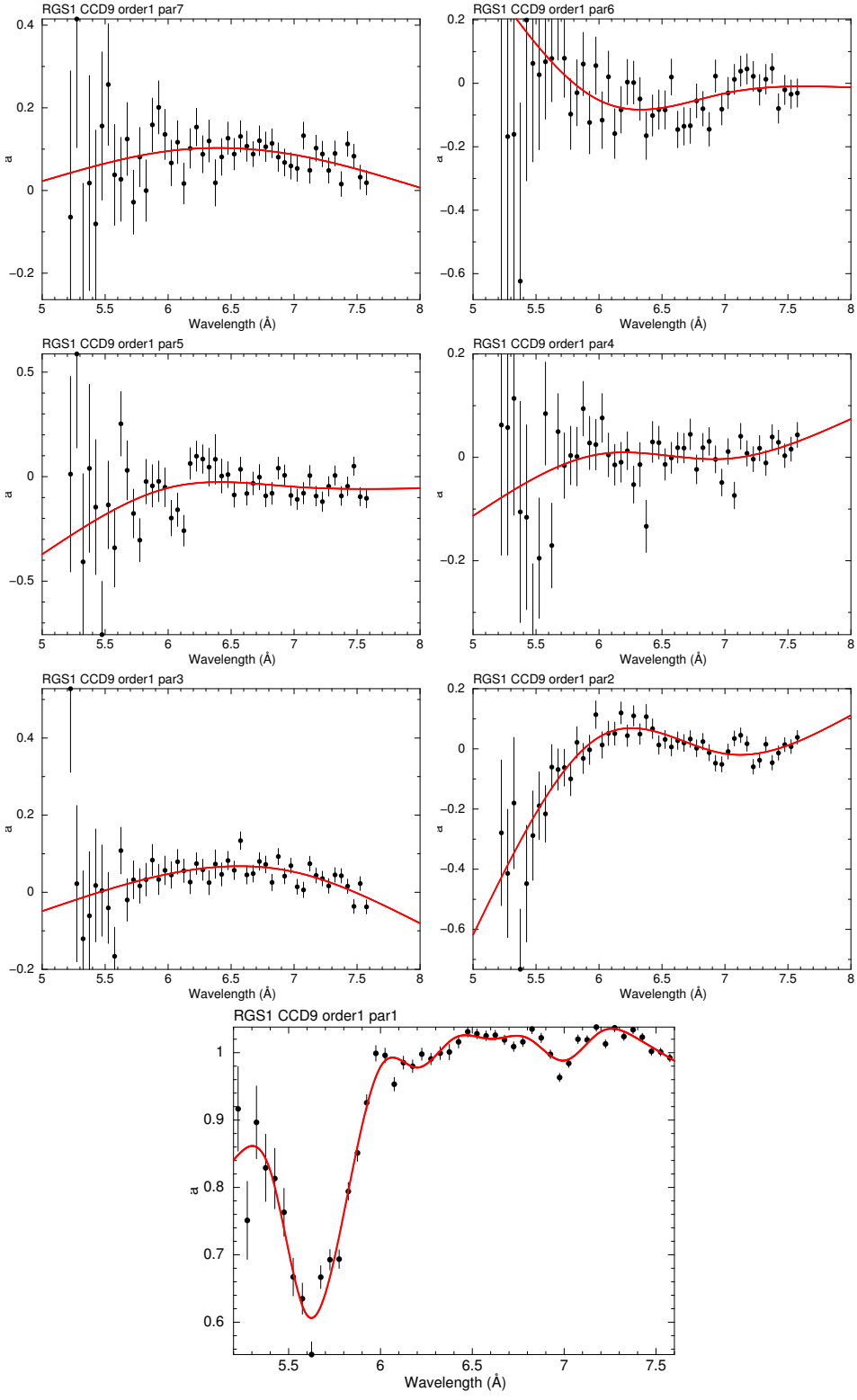

Figure 23: Continuation of previous figure.

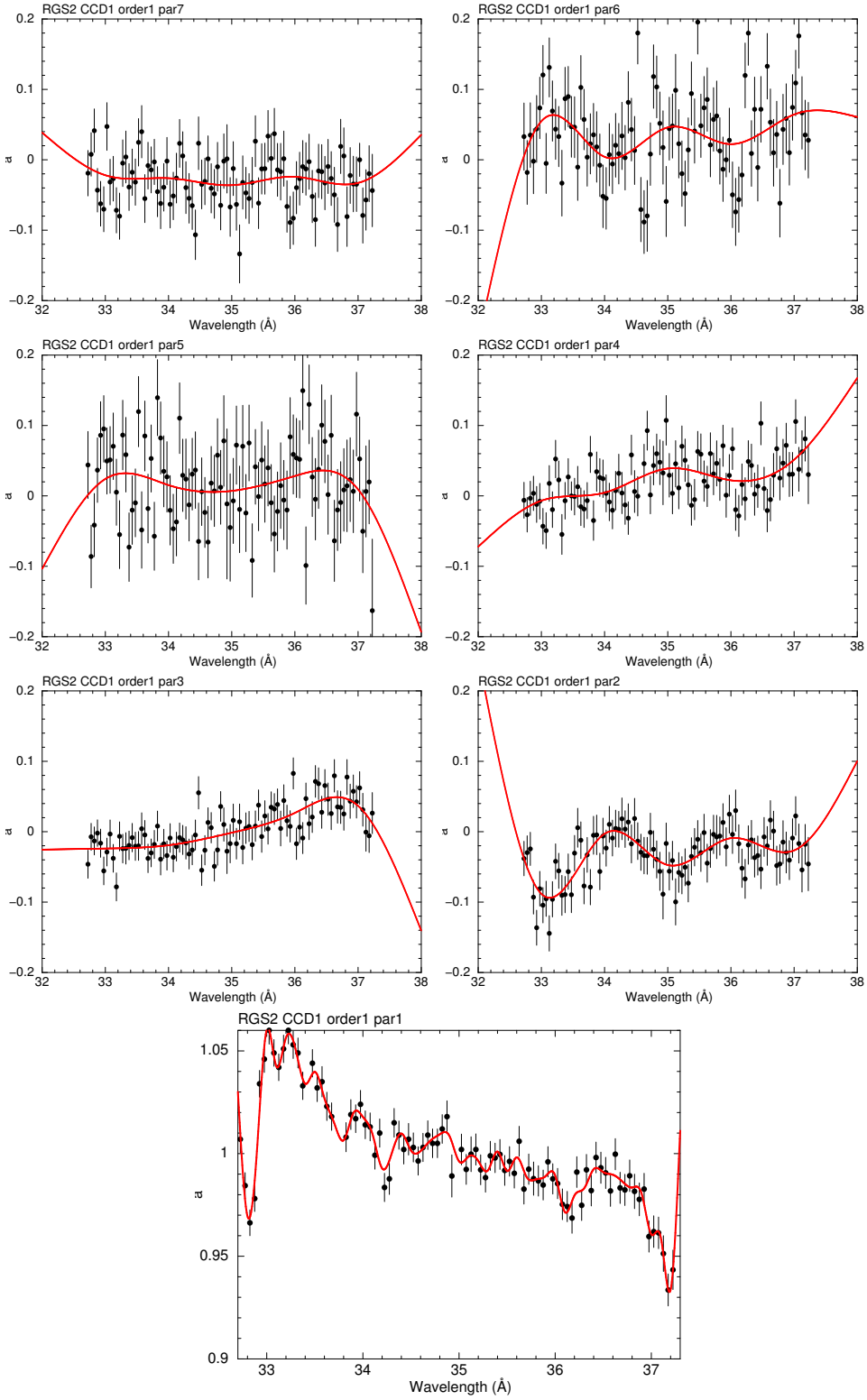

Figure 24: Continuation of previous figure.

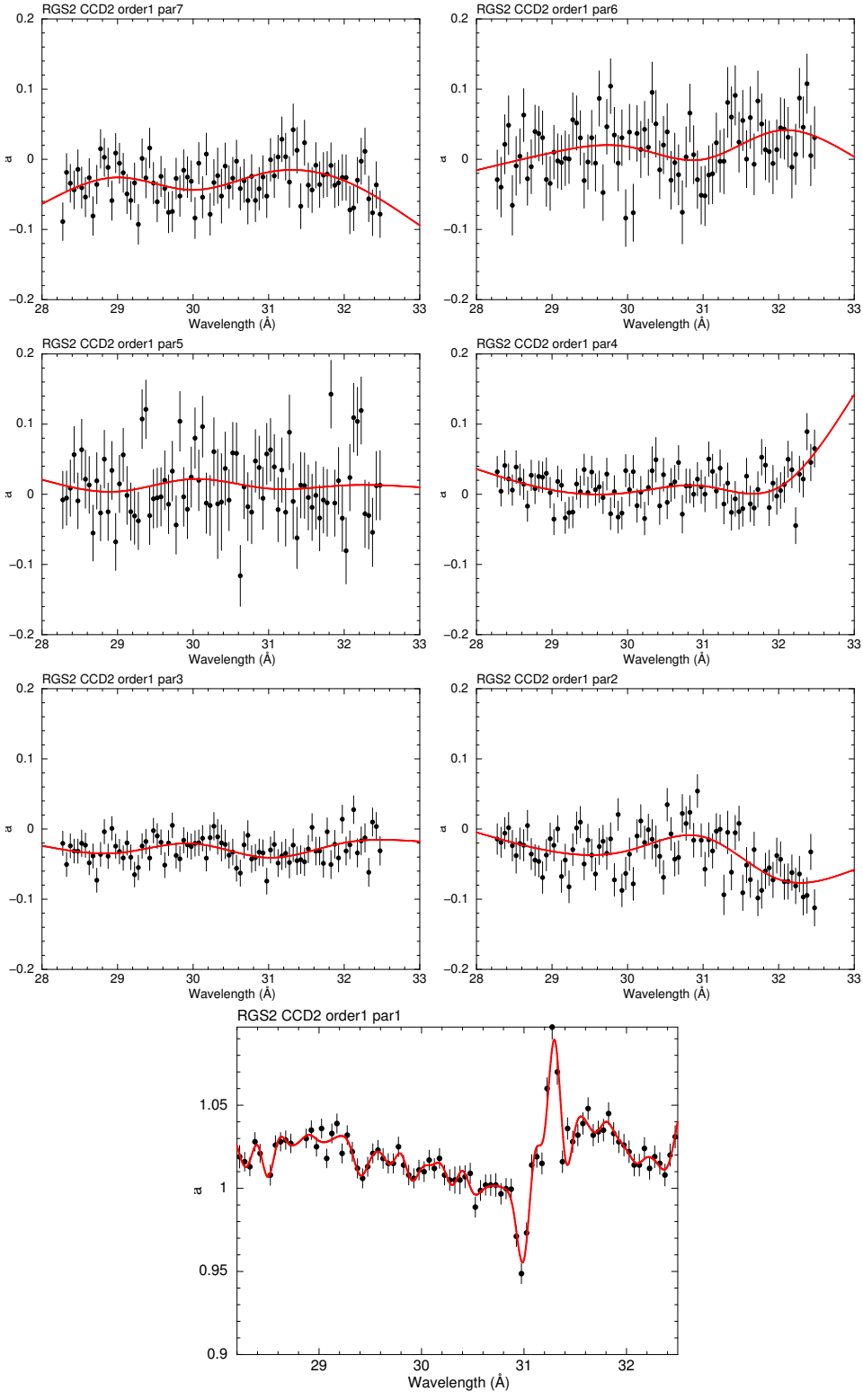

Figure 25: Continuation of previous figure.

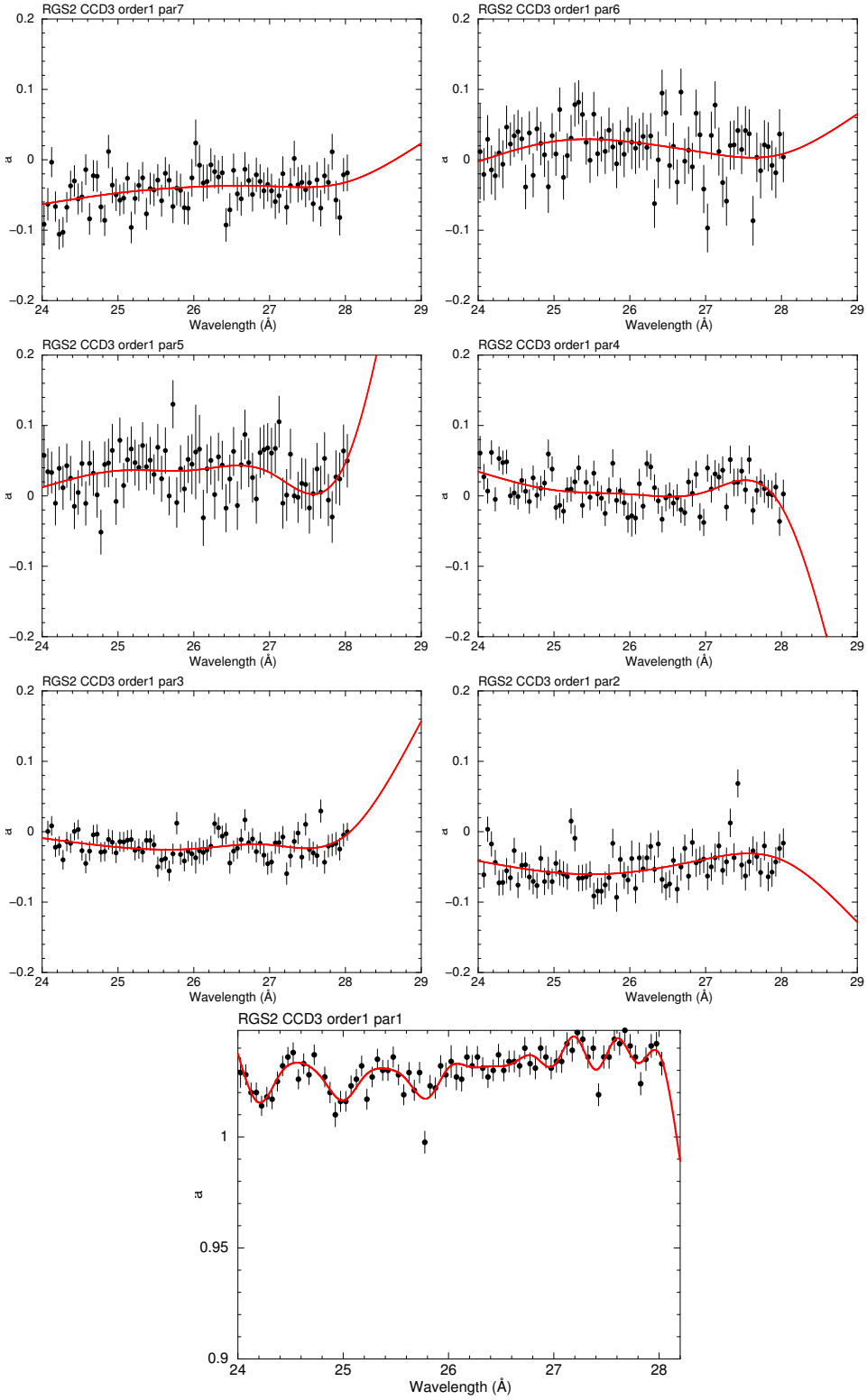

Figure 26: Continuation of previous figure.

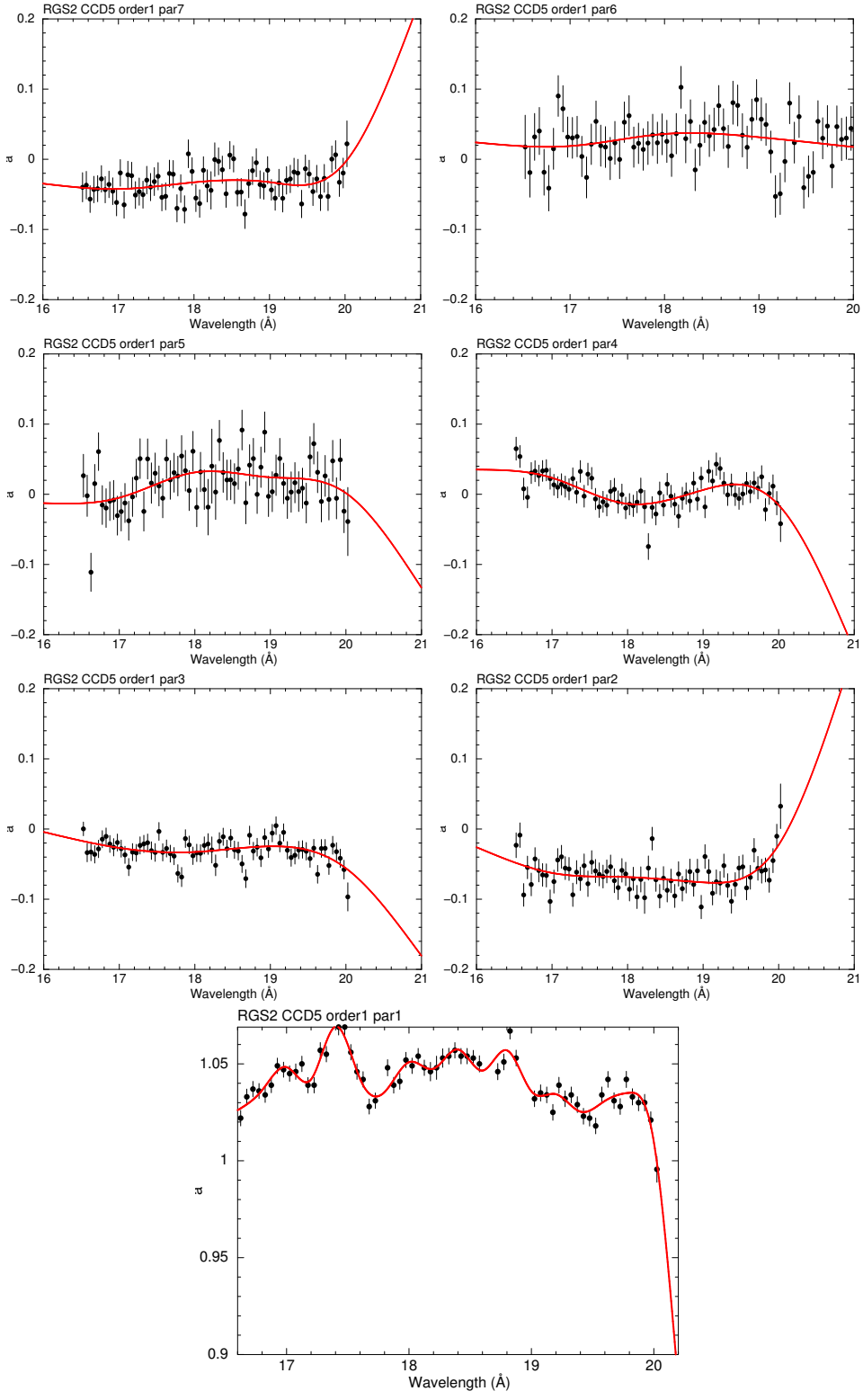

Figure 27: Continuation of previous figure.

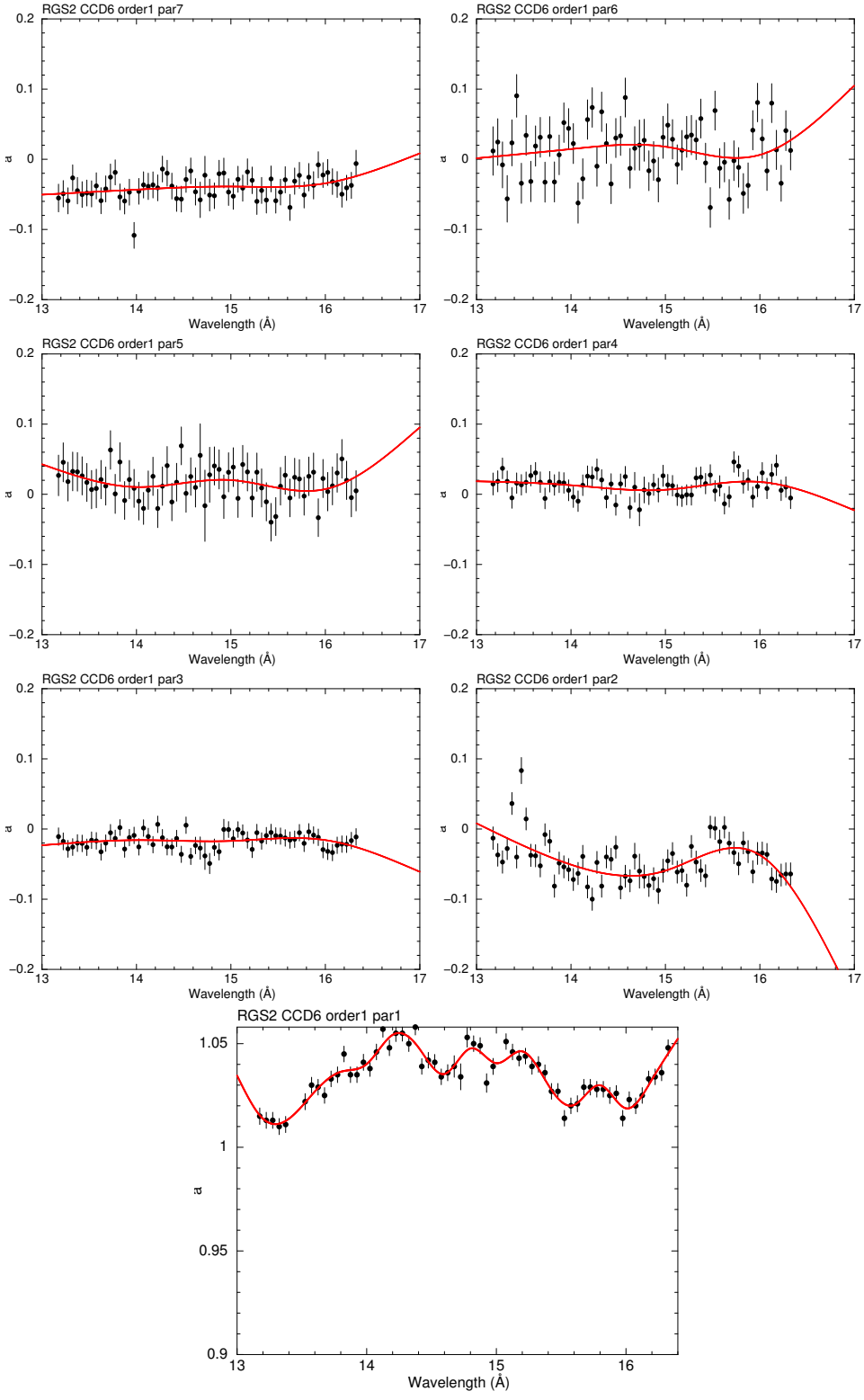

Figure 28: Continuation of previous figure.

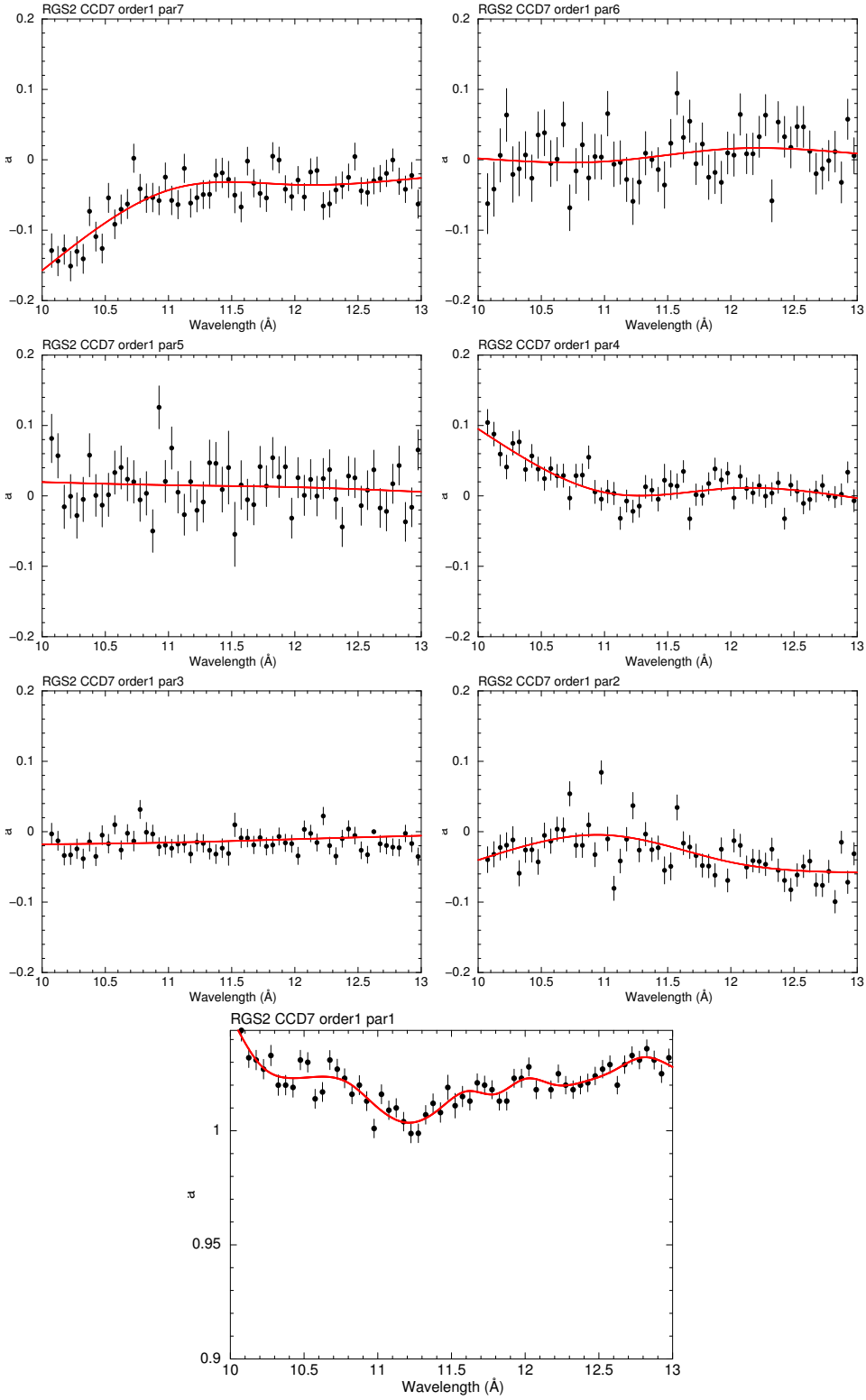

Figure 29: Continuation of previous figure.

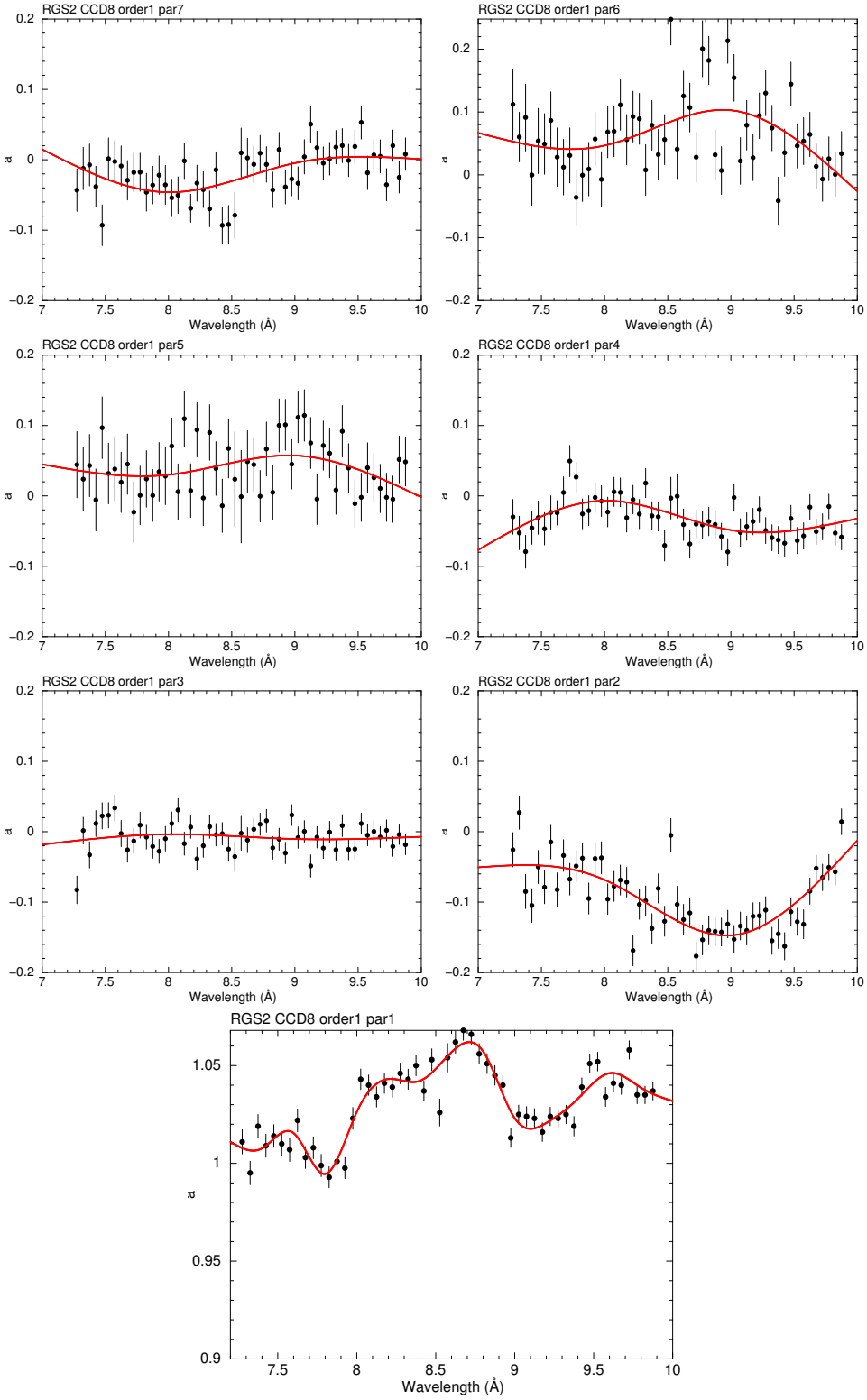

Figure 30: Continuation of previous figure.

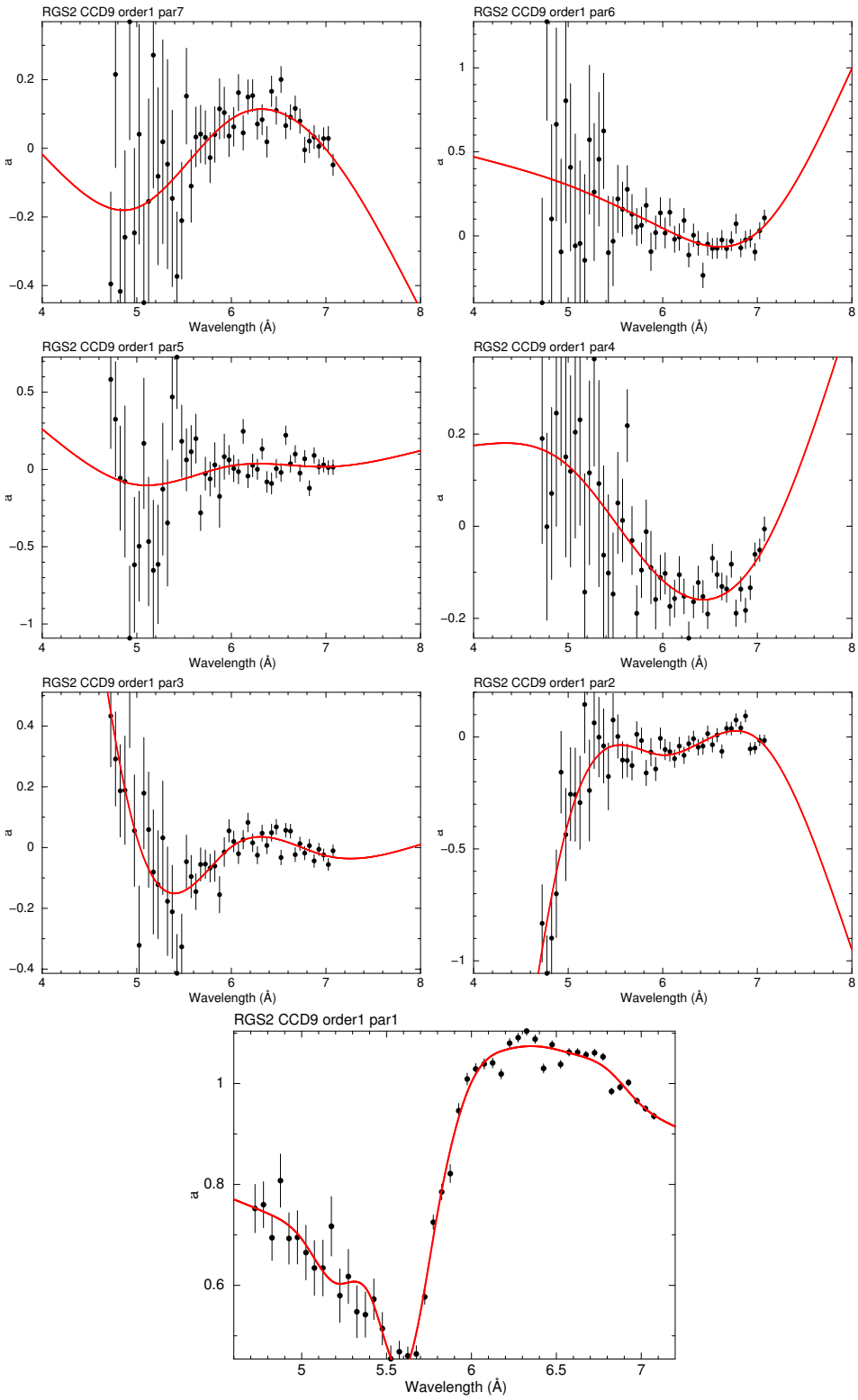

Figure 31: Continuation of previous figure.

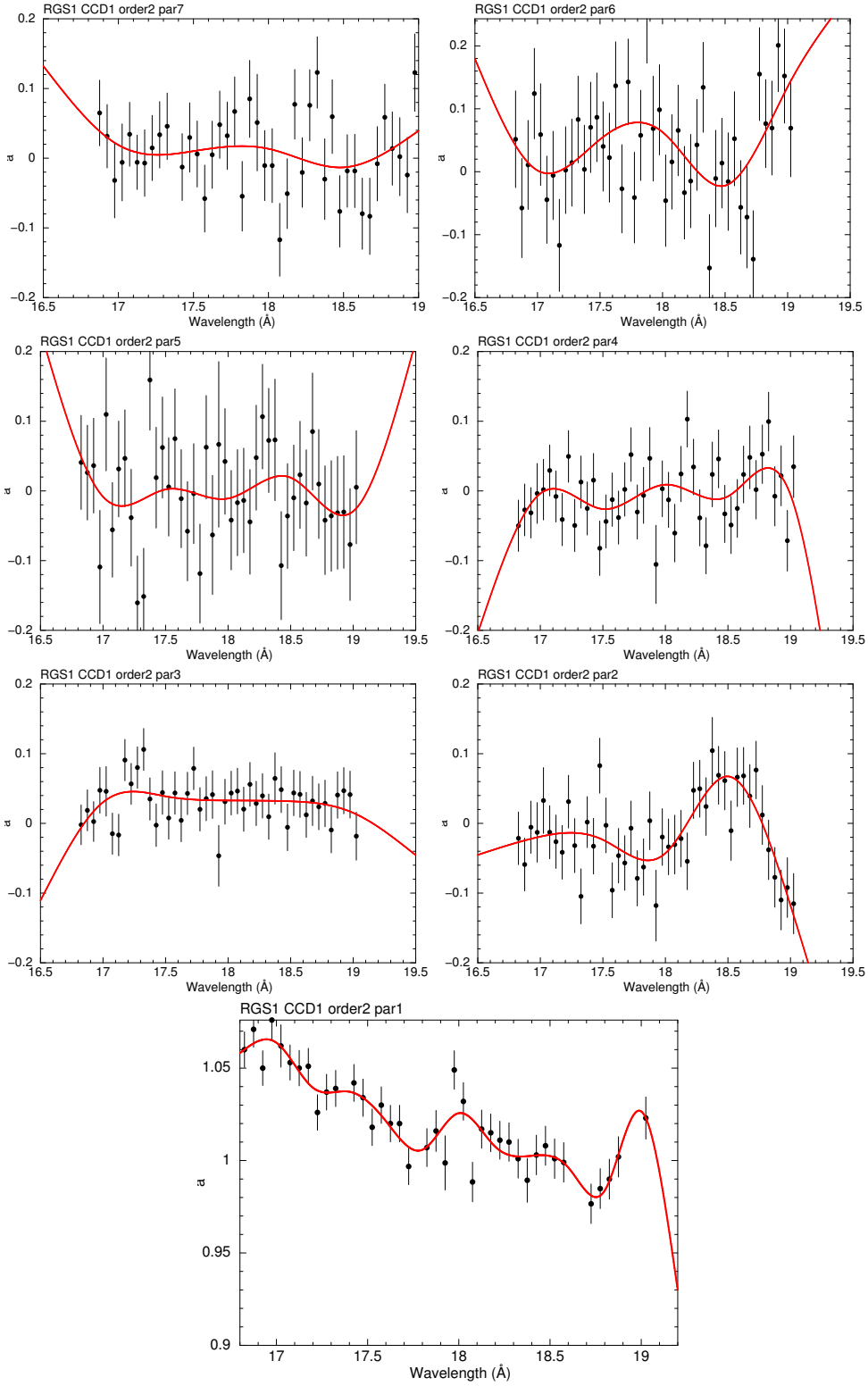

Figure 32: Continuation of previous figure.

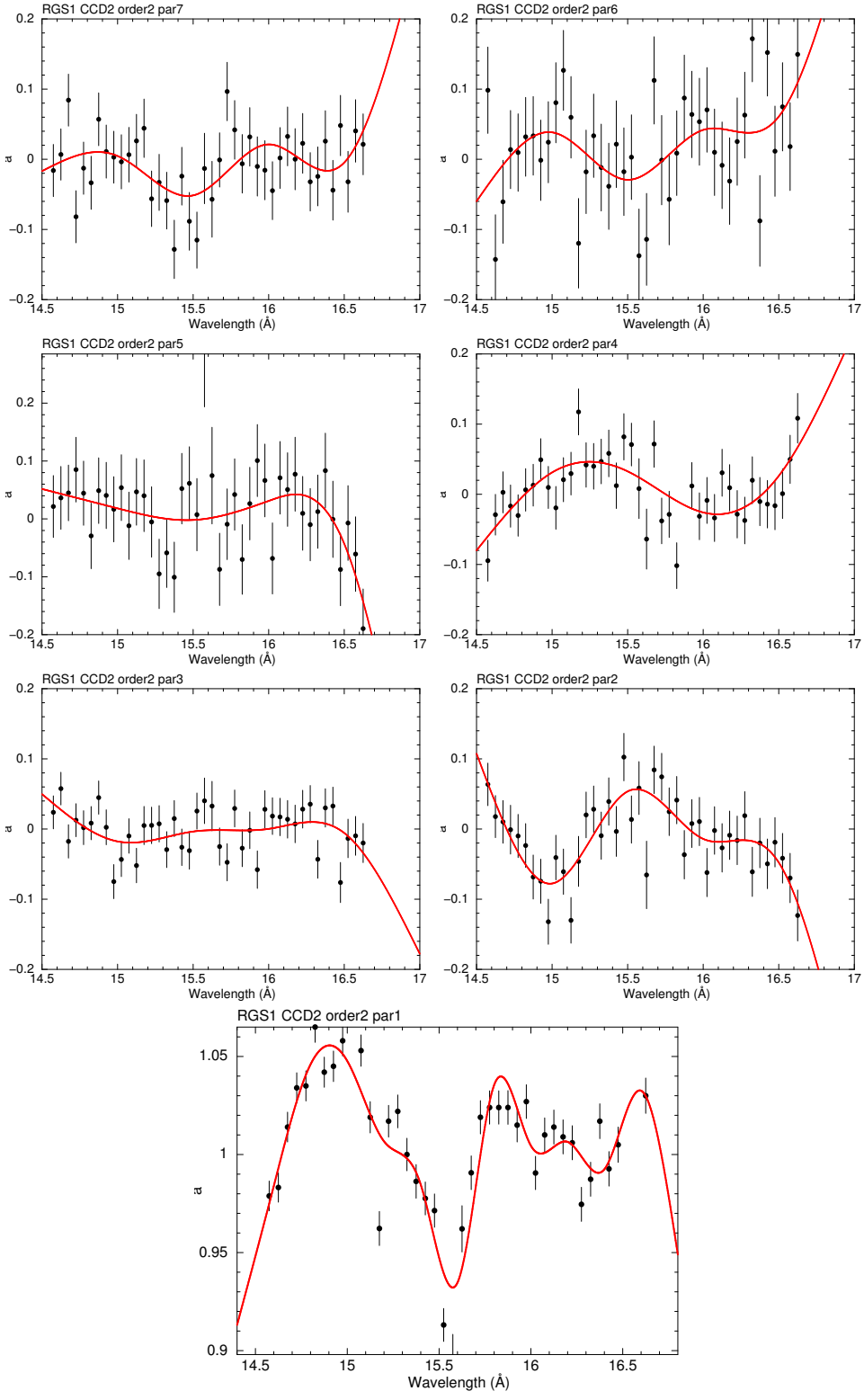

Figure 33: Continuation of previous figure.

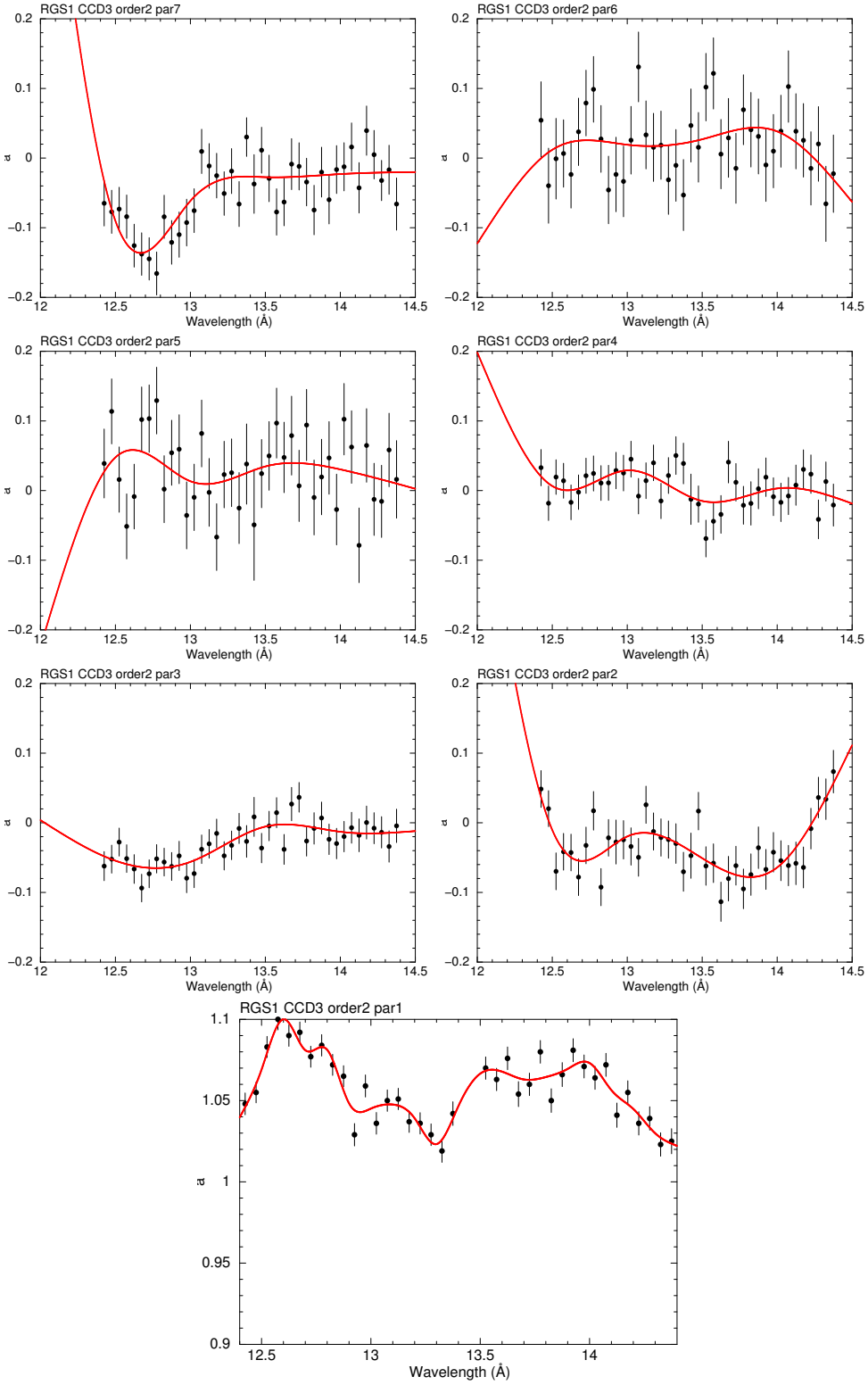

Figure 34: Continuation of previous figure.

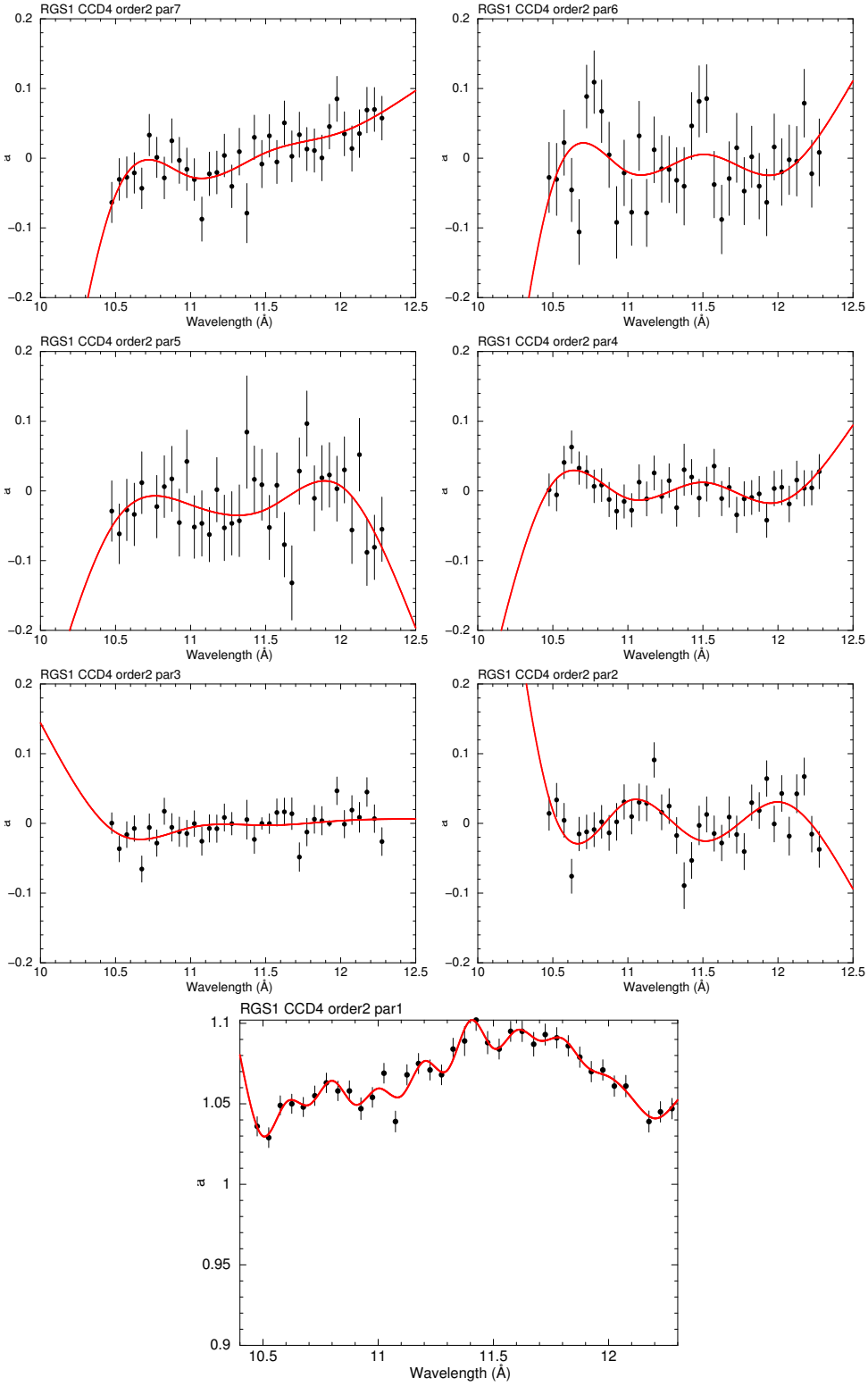

Figure 35: Continuation of previous figure.

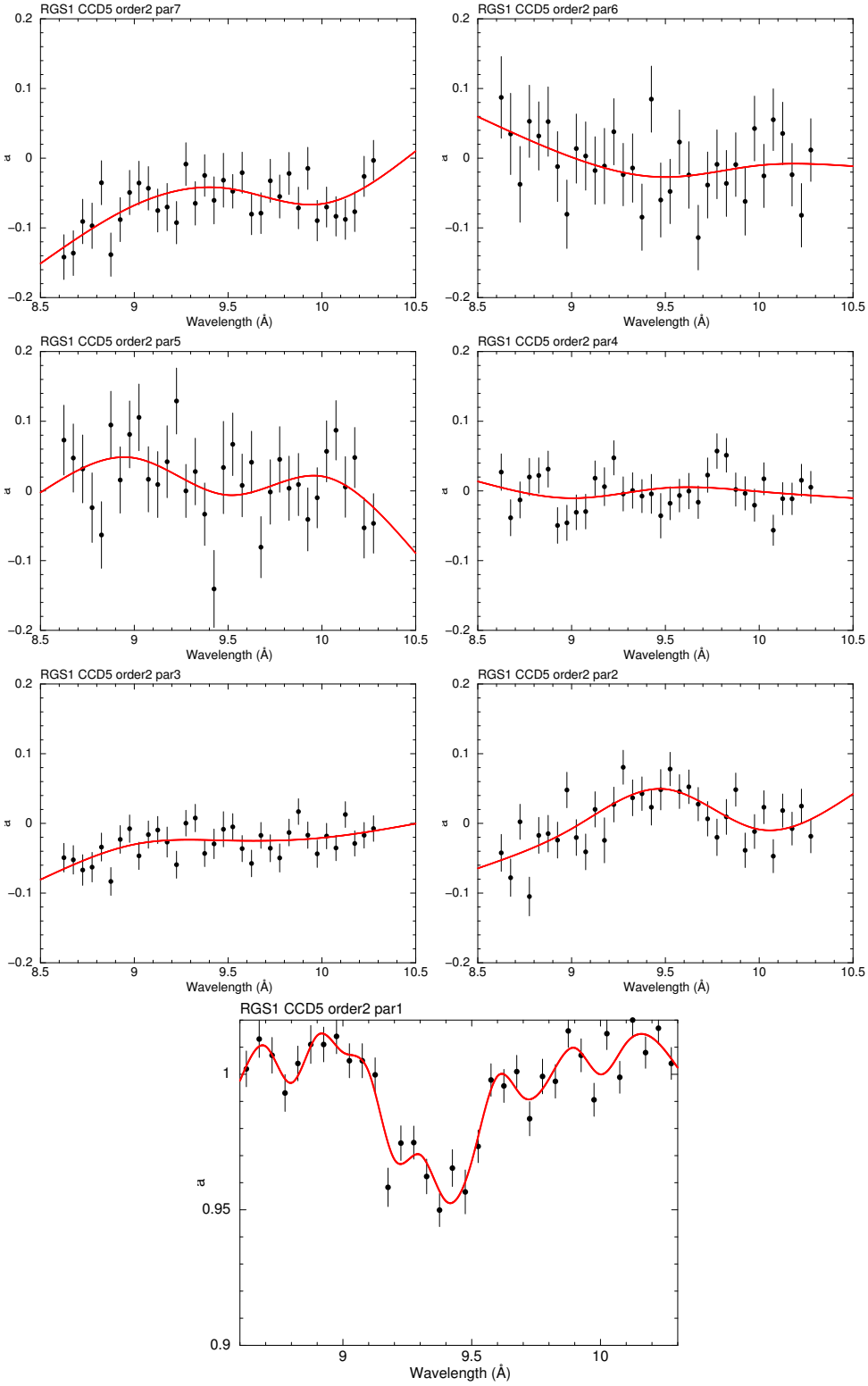

Figure 36: Continuation of previous figure.

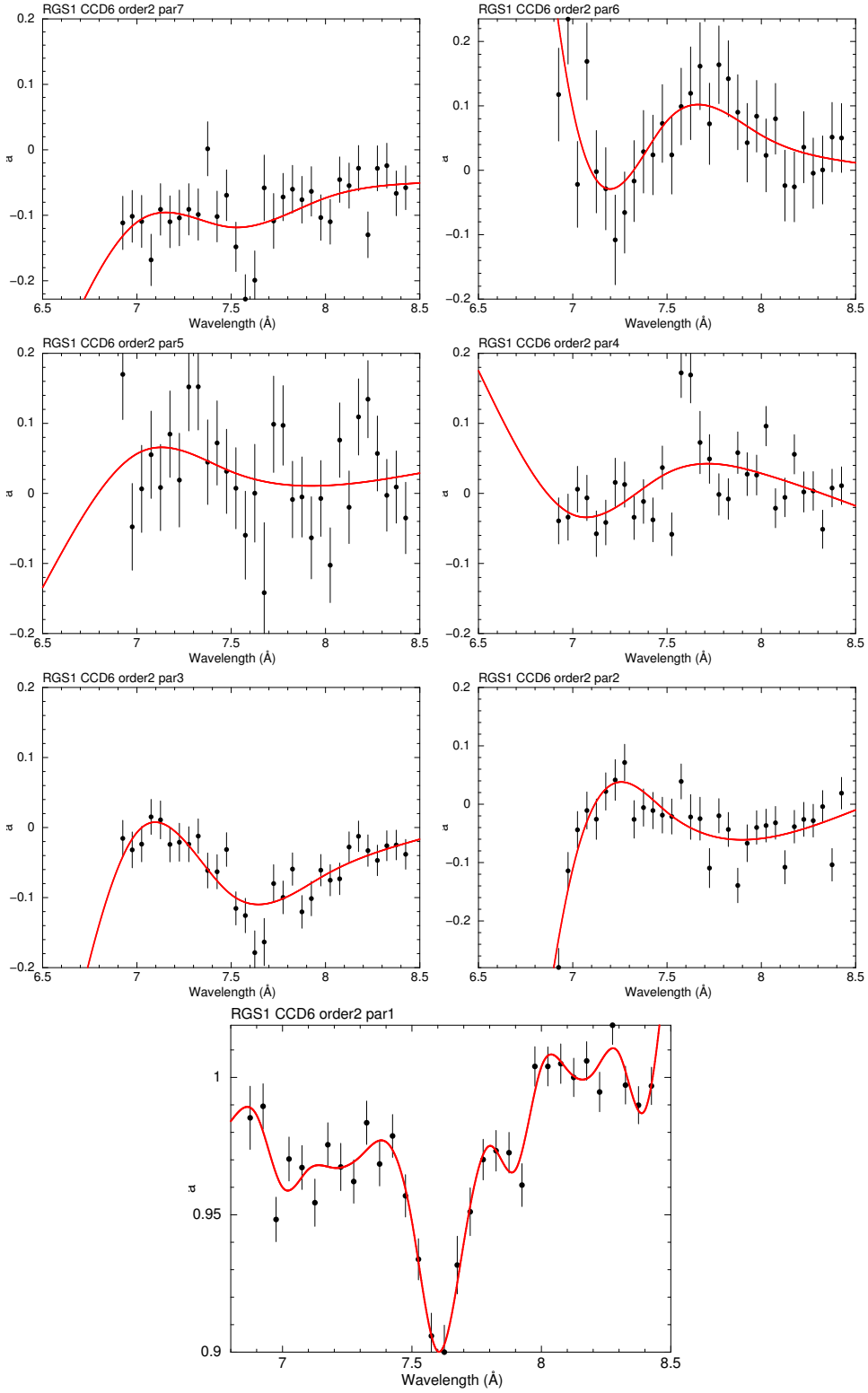

Figure 37: Continuation of previous figure.

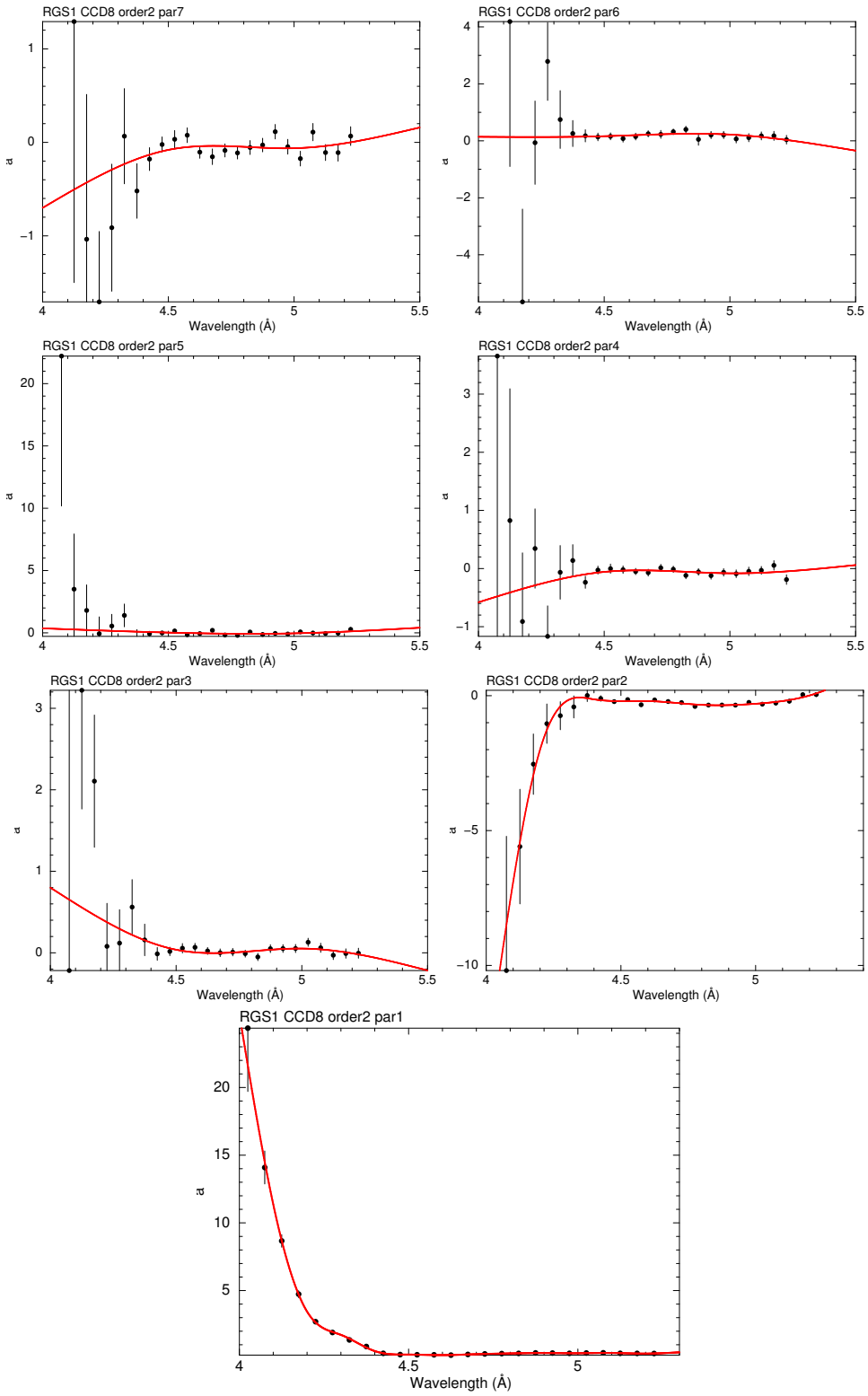

Figure 38: Continuation of previous figure.

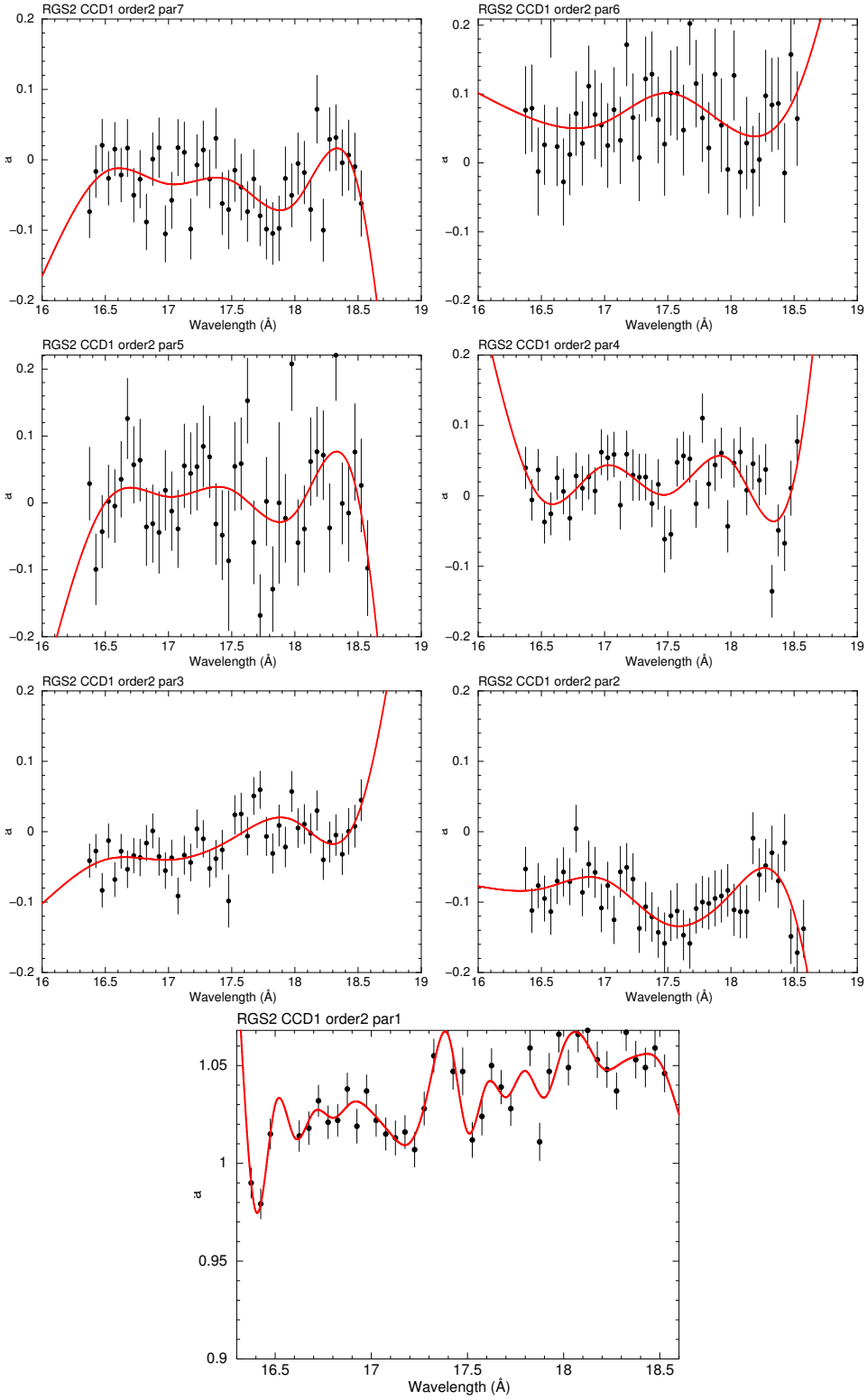

Figure 39: Continuation of previous figure.

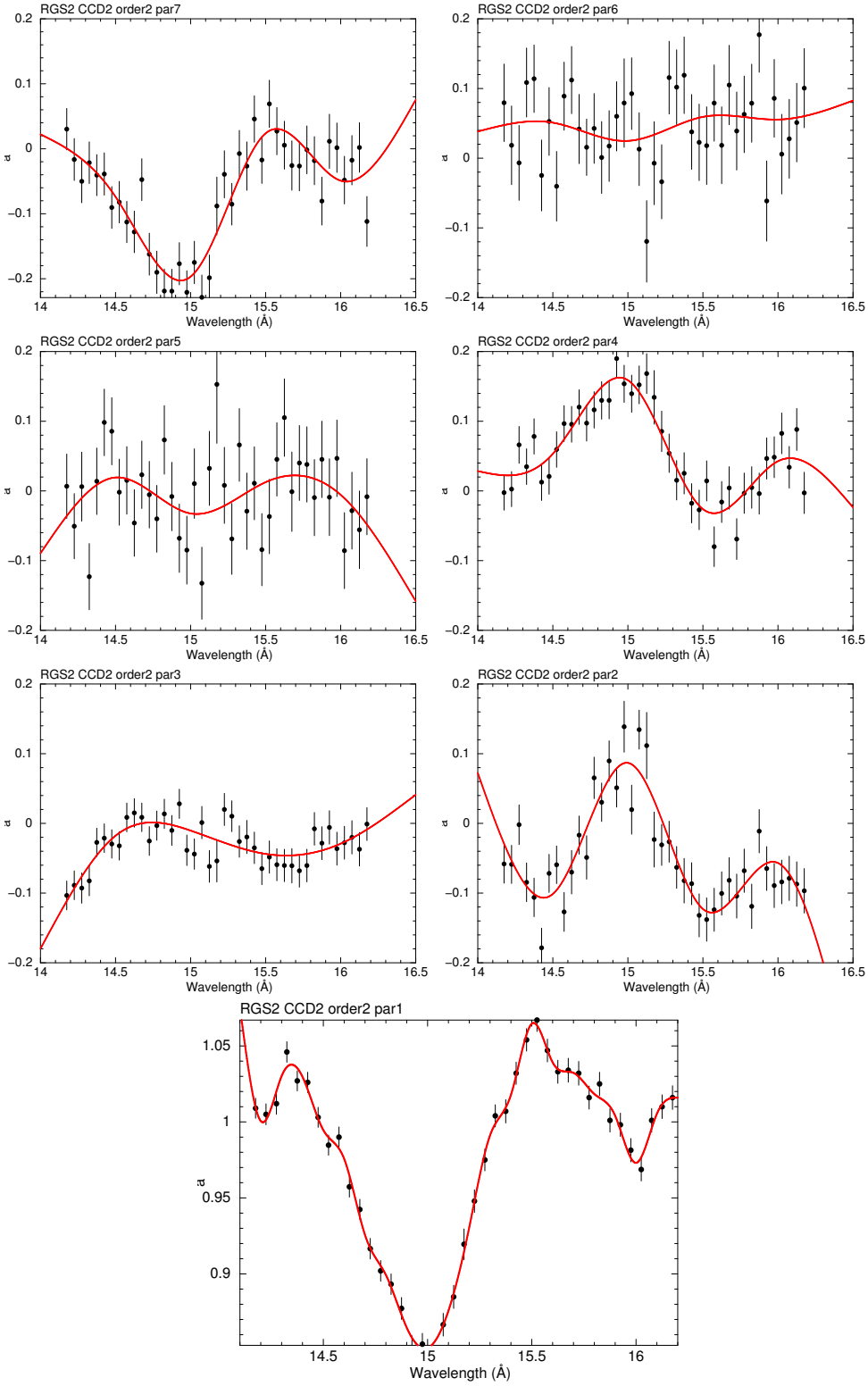

Figure 40: Continuation of previous figure.

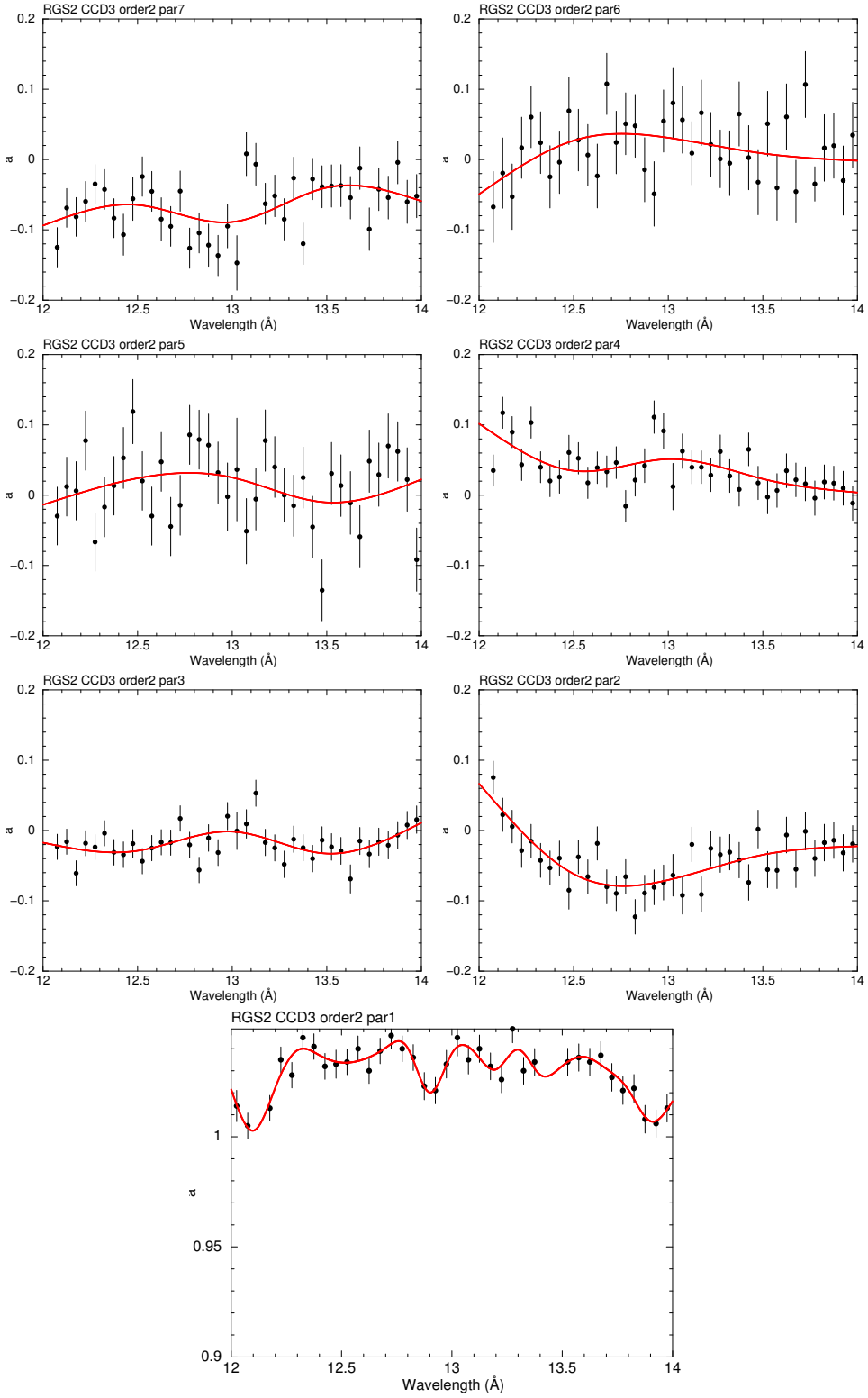

Figure 41: Continuation of previous figure.

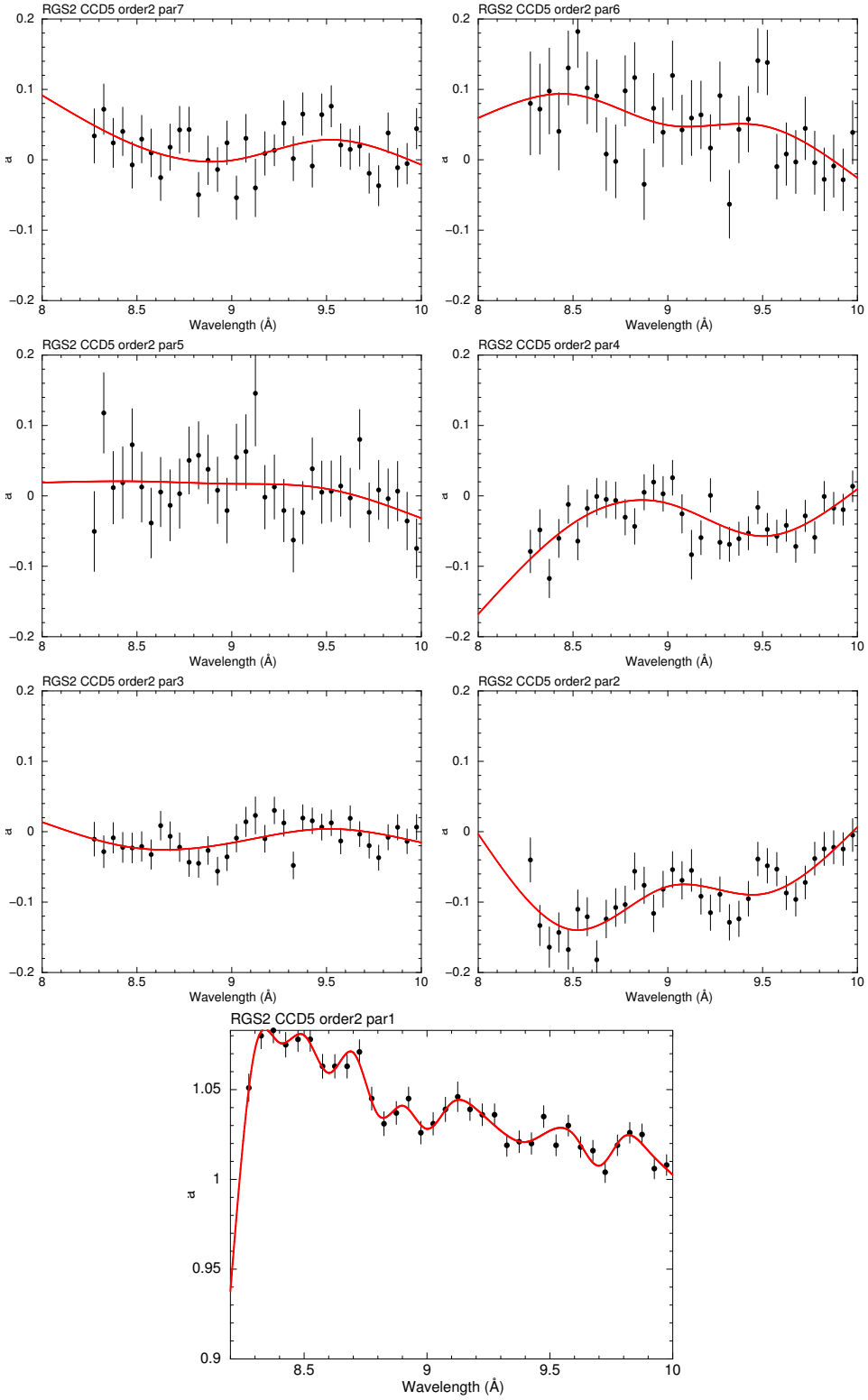

Figure 42: Continuation of previous figure.

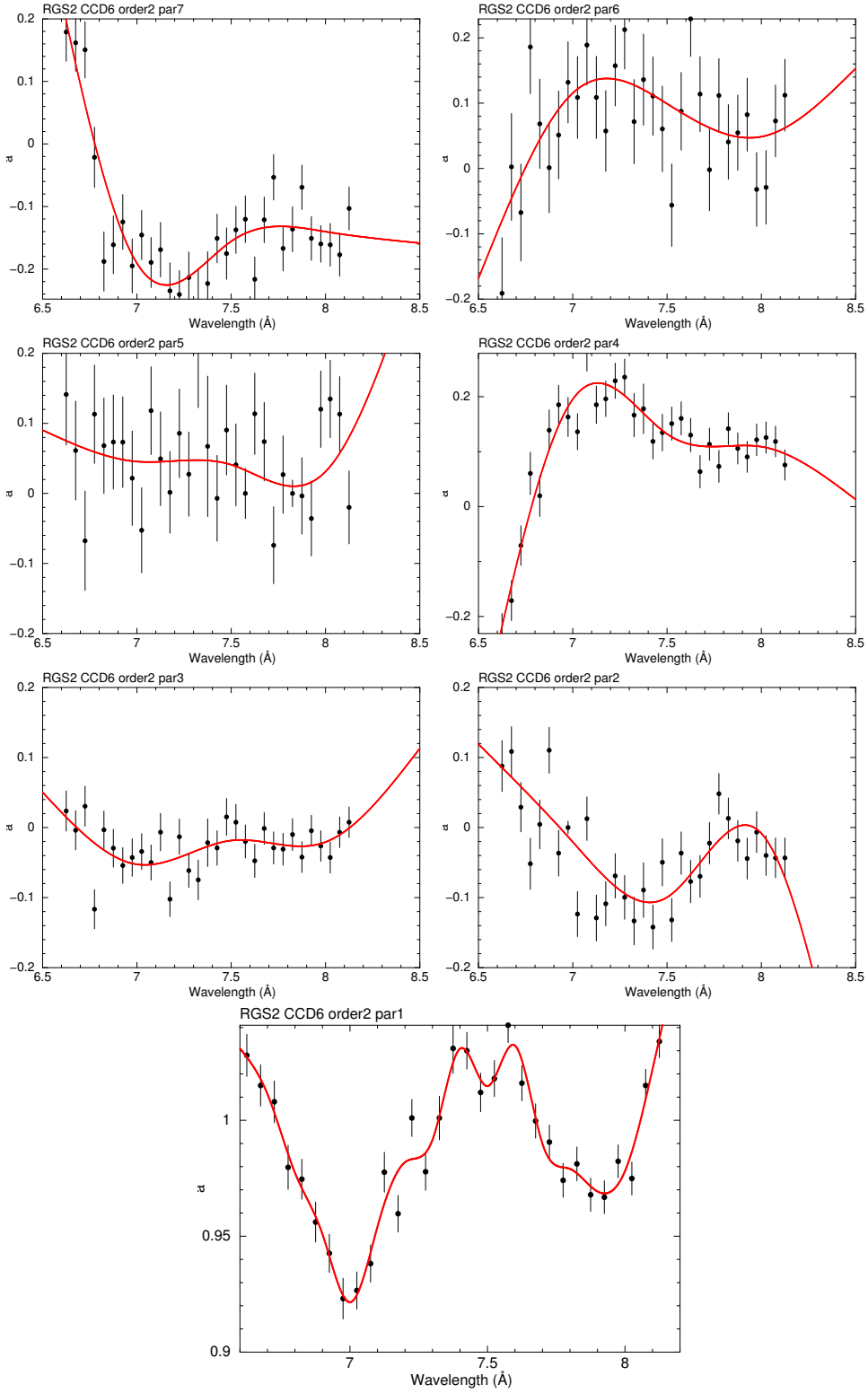

Figure 43: Continuation of previous figure.

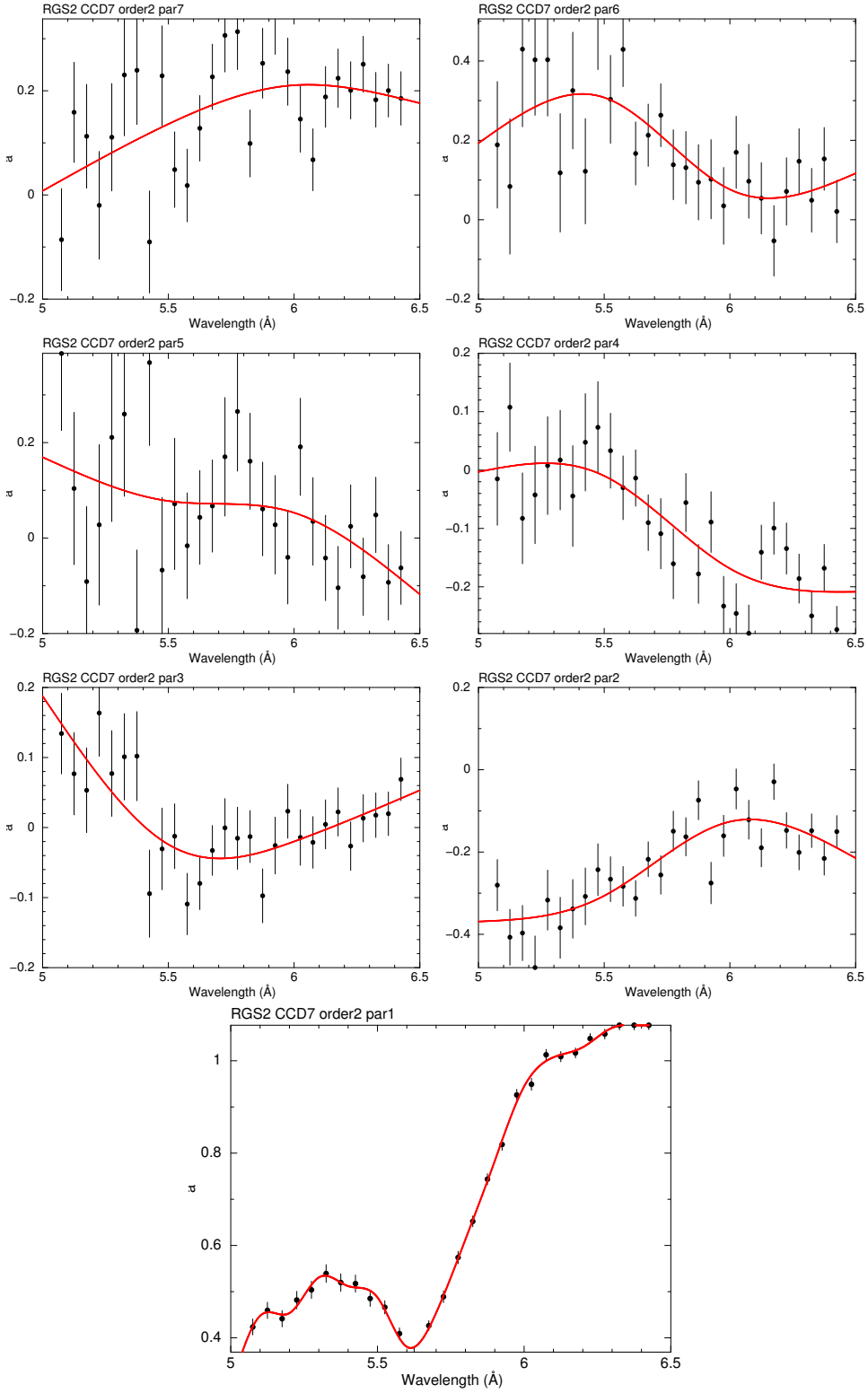

Figure 44: Continuation of previous figure.

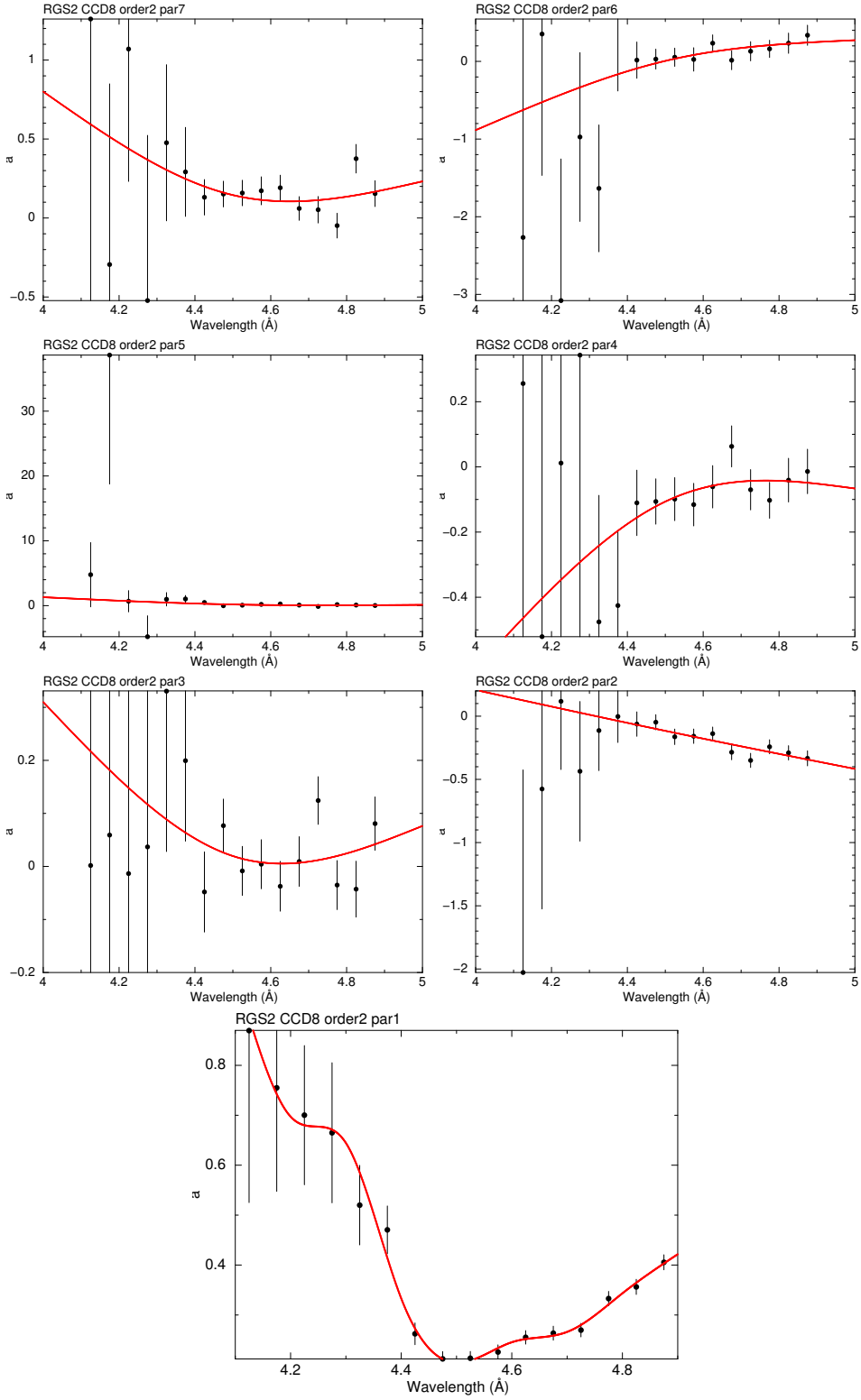

Figure 45: Continuation of previous figure.